POLITECNICO DI TORINO

Dipartimento di Ingegneria Meccanica e Aerospaziale
Master of Science in Aerospace Engineering

Master's Thesis

Development of a Generalized Inverse Beamforming tool for Aeroacoustic source imaging in Wind Tunnel and Computational Environments

Supervisors:
Prof. Francesco Avallone

Dr. Riccardo Zamponi

Candidate:
Alessandro Carriero
mat. 301581

Academic Year 2022/2023

The present work was conducted at the *Von Karmán Institute for Fluid Dynamics* as part of the *Short Training Programme*.

Alla mia famiglia.
A Federica.

ABSTRACT

In the realm of aeroacoustic applications, precise and detailed analysis of acoustic phenomena is essential for enhancing the comprehension of aerodynamic sound emission mechanisms and the design and performance of aerodynamic devices and systems, such as wings and engines. In this particular context, beamforming is currently receiving significant attention within the scientific community due to its ability to distinguish and measure acoustic sources through the use of phased arrays.

This study proposes the development of an innovative UI-based beamforming tool implementing the Generalized Inverse Beamforming (GIBF) technique, which is a promising method resolving coherent and incoherent sparse source distributions that especially occur in aerodynamics. This approach is designed to enable accurate and reliable measurements both in physical wind tunnels and Computational AeroAcoustics (CAA) simulations. Through a three-dimensional source-to-microphone propagation model, a novel three-dimensional source reconstruction approach is implemented and applied. To reconstruct the source, only the most significant eigenmodes are selected by an algorithm that decomposes the Cross-Spectral Matrix (CSM) into eigenvectors. The resulting linear system is then inverted using an iterative process that aims to promote sparsity by minimizing the $\mathcal{L}^1$ norm. Multipoles are all considered and detected simultaneously, reducing the solution's dependence on the specific source model imposed. This approach represents a substantial advancement with respect to the field's state-of art, enhancing the explanation of the physics behind the acoustic production. Furthermore, the propagation model is adjusted to incorporate the effects of convection of acoustic sources caused by the average flow. Additionally, in wind tunnel measurements, the presence of a boundary layer between the sources and the laboratory environment, where pressure measurements are conducted, is taken into account by implementing corrections.

Details on the implementation of GIBF and its practical applications in fictitious and real-world scenarios are presented, demonstrating its effectiveness in characterizing and interpreting acoustic events. The results showcase the framework's ability to offer deep insights into the origin and distribution of acoustic sources, thereby contributing to the enhancement of aerodynamic performance and noise reduction in various aeronautical applications.

Contents

List of Figures

List of Tables

Nomenclature

Acronyms

CAA	Computational AeroAcoustics
CSM	Cross Spectral Matrix of the microphone-recorded pressure signals
DNS	Direct Numerical Simulation
FFT	Fast Fourier Transform
FFW-H	Ffwocs Williams and Hawkings acoustic analogy
GIBF	Generalized Inverse Beamforming
IL	Intensity level
IRLS	Iterative Re-weighted Least Squares method
LEE	Linearized Euler's equations
LES	Large Eddy Simulation
PDE	Partial Differential Equation
PWL	Power level
SNR	Signal-to-noise ratio
SPL	Sound pressure level
UI	User interface
VKI	Von Karmán Institute for Fluid Dynamics (Belgium)
iBF	Iterative Bayesian Focusing

Greek letters

β	Reduction factor (GIBF)

$\boldsymbol{\zeta}$	Dipole's axis orientation
δ	Dirac's delta function
μ	Dynamic Viscosity
μ_R	Regularization factor (GIBF)
ω	Signal angular velocity
ϕ	Angular phase
ρ	Density
ε	Regularization parameter (GIBF)

Latin letters

$\mathbf{A}$	Transfer matrix (GIBF)
$\mathbf{I}$	Acoustic intensity
$\mathbf{n}$	Unitary vector normal to a surface
$\mathbf{T}$	Lighthill's stress tensor
$\mathbf{u}$	Velocity vector
$\mathcal{G}$	Green's function
$\mathcal{G}_0$	Free-field Green's function
$\mathcal{M}$	Molar mass
$\mathcal{R}$	Universal gas constant
Re_a	Acoustic Reynolds number
c_0	Speed of sound in the propagation region
k	Wave number
M	Mach number
p	Pressure
p_0	Time-averaged pressure of the medium
P_W	Acoustic power
q	Grid point's source amplitude

r	Absolute distance
s	Entropy per unit mass
T	Temperature
t	Time

Other symbols

$(\cdot)'$	Acoustic quantity
$(\cdot)_0$	Time-averaged quantity referred to medium
$(\cdot)_t$	Partial time-derivative
$(\cdot)_{\mathrm{RMS}}$	Root mean square
$\hat{(\cdot)}$	Fourier Transformed quantity
$\mathbf{x}$	Vector
$\mathbf{x}^{\mathrm{H}}$	Complex conjugate transpose of $\mathbf{x}$
$\mathbf{x}^{\mathrm{T}}$	Transpose of $\mathbf{x}$
∇	Nabla operator
∇^2	Laplacian
$\overline{(\cdot)}$	Time average (*statistics*)
i	Imaginary unit

Chapter1

INTRODUCTION

1.1 THE IMPORTANCE OF REDUCING AERODYNAMIC NOISE

Noise caused by the air transportation has garnered a considerable amount of attention and concern within recent years. This heightened focus can be attributed to the notable increase in the volume of air traffic, as well as the proximity of airports to urban centers, thus exacerbating the issue at hand. Aviation noise pollution has consequently emerged as an environmental and public health concern impacting a substantial number of individuals residing in Europe.

The field of psychoacoustics, a discipline dedicated to examining the subjective perception of sound in humans, has shed light on a myriad of pathologies that arise from consistent and prolonged exposure to aerodynamic noises. These pathologies encompass a range of detrimental effects, including but not limited to irritability, sleep disturbances, mental and cardiovascular ailments [1, 2], as well as impaired cognitive functions in children [3], particularly in the most severe instances.

For this rationale, there exist numerous global regulations [4, 5] that impose limitations on the sound generated by aeronautical operations, which occur in accordance with the so-called "balanced approach", which encompasses considering diverse facets:

- Mitigation of noise produced by aircraft, with the explicitly stated objective of diminishing, by 2050, acoustic discharges by 65% compared to the levels of 2000 [6];
- Management and planning of land usage, wherein the inclusion of noise insulation in residential structures may also be contemplated;
- Procedures aimed at diminishing noise, exemplified by the profiles of takeoff and landing during the flight;

- Restrictions imposed on the operation of airports, particularly during the hours of darkness, during which solely the most subdued aircraft may operate.

The possibility of reducing noise is strongly linked to knowledge of *where it is generated*. This is why having algorithms capable of determining it becomes essential in order to meet the above-mentioned challenges. Nowadays, this is done through *beamforming algorithms*, that exploit the signal processing of *phased microphone arrays*. In particular, among the most promising beamforming techniques there are *inverse methods*, capable of solving the acoustic field *all at the same time* hence intrinsically considering interference, a property that makes them preferable in aeroacoustic analysis.

1.2 OBJECTIVES OF THE THESIS

In this work, the author aims to develop a aeroacoustic beamforming tool featuring a graphical interface and implementing the *Generalized Inverse Beamforming* (GIBF), a inverse technique proposed by Suzuki [7] to localize and quantify noise sources within a region of interest. The work is developed on the following key points:

- Implementation of the algorithm in a user-friendly MATLAB app delivering to the researcher a fast and reliable beamforming analysis;
- Development of a multipole detection algorithm enabling dipole-beamforming;
- Implementation of corrections for convection velocity and shear layer in open-jet wind tunnel measurements;
- Extension to 3D source imaging;
- Investigation on the effects of regularization on the source strenght quantification;
- Application of the code on benchmarks and real-world measurements.

Chapter2

THEORETICAL BACKGROUND

This chapter will be dedicated to the review of theoretical concepts necessary for the understanding of the work here presented. The fundamentals of linear acoustics will be exposed in sec. 2.1, where the acoustic wave equation and its solution, through the use of the Green's function formalism, will be derived. In sec. 2.2, the equations of linear acoustics will be rewritten in their frequency-domain formulation. Then, the aerodynamic phenomena behind the *generation of noise* will be introduced in sec. 2.3 and formalised through the *Lighthill's analogy*.

2.1 LINEAR ACOUSTICS THEORY

Sound can be described as the fluctuation of pressure p' in a fluid over time and space, relative to an average pressure. This oscillation takes the form of a longitudinal wave that travels at a finite velocity, typically $340\,\mathrm{m\,s^{-1}}$ in air under standard conditions. The variation in pressure leads to a corresponding change in fluid velocity $\mathbf{u}'$. Consequently, the propagation of sound involves an *energy transfer*. The human ear is capable of perceiving vibrations with frequencies ranging from 20Hz to 20kHz.

2.1.1 Sound metrics

As effects of noise depend on its amplitude and on the capacity to transfer power to surfaces, one should quantify noise levels. In noise quantification, root mean square value of the acoustic pressure p'_{RMS} is what contributes to sound's effective amplitude

$$p'_{\mathrm{RMS}} = \sqrt{\lim_{T\to\infty} \frac{1}{T} \int_0^T (p(t) - p_0)^2 \,\mathrm{d}t} \tag{2.1}$$

Situation	SPL
Hearing threshold	0dB
Normal conversation	50dB
Noisy workplace	85dB
Live concert	105dB
Pain threshold	120dB
Jet take-off	140dB

Table 2.1: Typical situations and associated sound pressure levels (SPL) experienced.

The increase in noise level is clearly observed as sound pressure p' increases. In order to more accurately measure the magnitude of sound pressure, it is compared on a logarithmic scale with a reference pressure p_{REF}, which is the minimum pressure detectable by the human ear, equivalent to 20µPa. This is the definition of *sound pressure level* (SPL)

$$\mathrm{SPL} = 20 \log_{10} \left(\frac{p'_{\mathrm{RMS}}}{p_{\mathrm{REF}}} \right) \tag{2.2}$$

However, the ability of sound to transfer energy through wave motion is not solely dependent on the amplitude of the acoustic pressure. It is a function, in general, of the *acoustic intensity* $\mathbf{I} = \overline{p'\mathbf{u}'}$, i.e. time-averaged product of acoustic pressure and velocity. Acoustic intensity I_n is hence defined as

$$I_n = \mathbf{I} \cdot \mathbf{n} = \frac{1}{T} \int_0^T p'\mathbf{u}' \cdot \mathbf{n} \, \mathrm{d}t \tag{2.3}$$

On a logarithmic scale, one can define the *intensity level* (IL) as below:

$$\mathrm{IL} = 10 \log_{10} \left(\frac{I_n}{I_{\mathrm{REF}}} \right) \tag{2.4}$$

where $\mathbf{n}$ is the unitary vector normal to the surface and $I_{\mathrm{REF}} = 10^{-12}\mathrm{W\,m^{-2}}$ by convention.

The overall impact of an acoustic source in its surrounding field can be determined by calculating the *acoustic power*

$$P_W = \int_S \mathbf{I} \cdot \mathbf{n} \, \mathrm{d}S \tag{2.5}$$

where integration has eliminated the dependence on the distance of the receiver, as opposed to SPL, whose value is a function of the listener's location. Consequently, the *acoustic power level* (PWL) is defined as:

$$\mathrm{PWL} = 10 \log_{10} \left(\frac{P_W}{P_{W,\mathrm{REF}}} \right) \tag{2.6}$$

with $P_{W,\mathrm{REF}} = 10^{-12}\mathrm{W}$.

2.1.2 Acoustic wave equation

In acoustic waves, which represent a small perturbation with respect to the pressure of the medium, the significant length scale is the wavelength λ, and the acoustic Reynolds number is defined as

$$\mathrm{Re}_a = \frac{\lambda c_0 \rho_0}{\mu} \tag{2.7}$$

Since for a harmonic wave in air at standard temperature, for not too high emission frequencies, we have $\mathrm{Re}_a \gg 1$, *viscous effects are negligible* in sound propagation. Thus, *Euler's equations* are considered to be appropriate for elucidating acoustic phenomena:

$$\begin{cases} \rho_t + \nabla \cdot (\rho \mathbf{u}) = Q^{(m)} \\ \rho \left(\mathbf{u}_t + \mathbf{u} \cdot \nabla \mathbf{u} \right) = -\nabla p + \rho \mathbf{f} \\ \rho T \left(s_t + \mathbf{u} \cdot \nabla s \right) = Q^{(w)} \end{cases} \tag{2.8}$$

where $Q^{(m)}$ is the mass injection per unit time and volume (e.g. the motion of a membrane can be modeled as a periodic mass injection and subtraction), $\mathbf{f}$ is a volume force and $Q^{(w)}$ is a thermal power injection per unit volume. The *equation of state* is to be incorporated to the system (2.8):

$$\frac{p}{\rho} = \frac{\mathcal{R}}{\mathcal{M}} T \tag{2.9}$$

Because sound is intended as a relatively small perturbation in the neighbourhood of reference pressure p_0, the following relations can be written

$$\begin{aligned} p &= p_0 + p' \\ \rho &= \rho_0 + \rho' \\ s &= s_0 + s' \\ \mathbf{u} &= \mathbf{u}_0 + \mathbf{u}' \end{aligned}$$

where acoustic quantities are negligible compared to reference values. Therefore, for an homogeneous medium ($p_0, \rho_0, s_0, \mathbf{u}_0$ being constant), in absence of thermal sources ($Q^{(w)} = 0$), the Euler's equations in (2.8) can be linearized as follows, leading to the *Linearized Euler's equations* (LEE) for a homogeneous flow-field:

$$\begin{cases} \rho'_t + \mathbf{u}_0 \cdot \nabla \rho' + \rho_0 \nabla \cdot \mathbf{u}' = Q^{(m)} \\ \rho_0 \left(\mathbf{u}'_t + \mathbf{u}_0 \cdot \nabla \mathbf{u}' \right) = -\nabla p' + \rho_0 \mathbf{f} \\ \rho_0 T_0 \left(s'_t + \mathbf{u}_0 \cdot \nabla s' \right) = 0 \end{cases} \tag{2.10}$$

with the *linearized equation of state* being valid:

$$\frac{p'}{p_0} = \frac{T'}{T_0} + \frac{\rho'}{\rho_0} \tag{2.11}$$

Eq. (2.10) can be combined to obtain the *convective wave equation* for the acoustic pressure $p'(\mathbf{x}, t)$:

$$\frac{1}{c_0^2}\left(\frac{\partial}{\partial t} + \mathbf{u}_0 \cdot \nabla\right)^2 p'(\mathbf{x}, t) - \nabla^2 p'(\mathbf{x}, t) = \frac{\partial}{\partial t} Q^{(m)}(\mathbf{x}, t) - \rho_0 \nabla \cdot \mathbf{f}(\mathbf{x}, t) \tag{2.12}$$

When pressure fluctuations propagate in a still fluid ($\mathbf{u}_0 = 0$), motion is governed by the well-known *acoustic wave equation*:

$$\frac{1}{c_0^2}\, p'_{tt}(\mathbf{x}, t) - \nabla^2 p'(\mathbf{x}, t) = Q_t^{(m)}(\mathbf{x}, t) - \rho_0 \nabla \cdot \mathbf{f}(\mathbf{x}, t) \tag{2.13}$$

The equation above is *linear partial differential equation* PDE *with constant coefficients*, whose solution is generally a sum of *wave functions* of the type:

$$p'_i(\mathbf{x}, t) = A_i(\mathbf{x} - \mathbf{x}_{0,i}) \cos\left[g(\|\mathbf{x} - \mathbf{x}_{0,i}\| \pm c_0 t) + \phi_i\right] \tag{2.14}$$

where subscript i denotes a generic wave in the domain and $x_{0,i}$ stands for the point where the perturbation arises, while ϕ_i accounts for the phase difference due to different emission times. These wave functions exhibit the following distinct characteristics:

- When waves pass through one another, they don't influence each other. This phenomenon is named *superposition principle*;
- The waves' propagation speed c_0 remains constant and is unaffected by the wave's intensity;
- The incident waves sum up with the reflected waves they produced.

The acoustic field cannot be adequately described solely by the wave equation formulated for p'. The determination of the acoustic velocity u' corresponding to the acoustic pressure field requires the coupling of the *acoustic momentum equation* already shown in eq. (2.10)

$$\rho_0 \left(\mathbf{u}'_t + \mathbf{u}_0 \cdot \nabla \mathbf{u}'\right) = -\nabla p' + \rho_0 \mathbf{f} \tag{2.15}$$

ultimately leading to the determination of the acoustic intensity $\mathbf{I}$. Indeed, the acoustic velocity $\mathbf{u}'$ plays a crucial role in determining the acoustic intensity's magnitude: the more $\mathbf{u}'$ is significant and in-phase with p', the greater the acoustic intensity I is, resulting in a more powered acoustic field. In still fluid conditions ($\mathbf{u}_0 = 0$), it is trivial to show that the acoustic velocity field is held by

$$\mathbf{u}'_t = -\frac{1}{\rho_0}\nabla p' + \mathbf{f} \tag{2.16}$$

The *acoustic momentum equation* (2.16) is frequently adopted to link the vibration of a surface to the subsequent sound production. In fact, a moving surface can be modeled as a domain border where a boundary condition applies. This is the case of a *loudspeaker*: the acoustic field is hence governed by the *homogeneous wave equation* (because the domain is free of physical sources):

$$\frac{1}{c_0^2}\, p'_{tt}(\mathbf{x},t) - \nabla^2 p'(\mathbf{x},t) = 0 \qquad \text{in } \Omega \tag{2.17}$$

with boundary conditions (representing a non-penetration condition on solid boundaries)

$$\mathbf{u}' \cdot \mathbf{n} = \mathbf{u}_b \cdot \mathbf{n} \qquad \text{on } \partial\Omega_b \tag{2.18}$$

where $\partial\Omega_b$ stands for the domain's solid boundary, $\mathbf{u}_b$ is its local instant velocity and $\mathbf{n}$ the unitary vector locally normal to the surface.

2.1.3 Green's function and integral solution to the wave equation

The solution of non-homogeneous PDE can be achieved by utilizing the Green's functions formalism. Application of this method can be contemplated in the context of solving the non-homogeneous wave equation (2.13). Notably, the Green's function exhibits a distinct dependence on the considered PDE and the associated boundary conditions.

Let $\mathcal{L}$ be the *wave operator*:

$$\mathcal{L} \equiv \frac{1}{c_0^2}\frac{\partial^2}{\partial t^2} - \nabla^2 \tag{2.19}$$

and $F(\mathbf{x},t)$ be the *forcing term* in eq. (2.13), i.e. the sum of every single contribution on the right side of the equation. Thus, it is possible to rewrite the wave equation in (2.13) as

$$\mathcal{L}[p'(\mathbf{x},t)] = f(\mathbf{x},t) \qquad \text{in } \Omega \tag{2.20}$$

with BC:

$$\mathbf{n} \cdot \nabla p' + b p' = 0 \qquad \text{on } \partial\Omega \tag{2.21}$$

where $\partial\Omega$ represents physical boundaries, that can scatter and emit waves. Theoretically, the Green's function $\mathcal{G}$ is found as the solution to the associated differential problem:

$$\begin{cases} \mathcal{L}[\mathcal{G}(\mathbf{x},t;\mathbf{y},\tau)] = \delta(\mathbf{x}-\mathbf{y})\delta(t-\tau) \qquad \text{in } \Omega \\ \mathbf{n} \cdot \nabla \mathcal{G} + b\mathcal{G} = 0 \qquad \text{on } \partial\Omega \end{cases} \tag{2.22}$$

where $\delta(\mathbf{x}-\mathbf{y})$ and $\delta(t-\tau)$ are the Dirac's function centered in $\mathbf{y}$ and τ respectively. Green's function $\mathcal{G}$ represents the causal response at position $\mathbf{x}$ and time t, resulting from an impulse emitted at time T by a point source located at position $\mathbf{y}$. A Green's function that satisfies the conditions surrounding the specific problem being considered is referred to as a *tailored Green's function* $\mathcal{G}$. The calculation of this function is not straightforward, as it relies on the specific geometry of the domain and the solid walls it encompasses, and it may not always exist analytically. It enables the formal solution to the differential problem:

$$p'(\mathbf{x},t) = \int_{-\infty}^{+\infty} \int_{\Omega} f(\mathbf{y},\tau)\mathcal{G}(\mathbf{x},t;\mathbf{y},\tau)\mathrm{d}^3\mathbf{y}\mathrm{d}\tau \tag{2.23}$$

When the Green's function is known only in the absence of walls, namely *free-field Green's function* $\mathcal{G}_0$, the formal solution also involves the evaluation of a surface integral to account for solid boundaries. In this scenario, the solution can be expressed as follows:

$$\begin{aligned} p'(\mathbf{x},t) = \int_{-\infty}^{+\infty} \int_{\Omega} f(\mathbf{y},\tau)\mathcal{G}_0(\mathbf{x},t;\mathbf{y},\tau)\ \mathrm{d}^3\mathbf{y}\mathrm{d}\tau \\ - \int_{-\infty}^{+\infty} \int_{\partial\Omega} (p'\nabla\mathcal{G}_0 - \mathcal{G}_0\nabla p') \cdot \mathbf{n}\ \mathrm{d}^2\mathbf{y}\mathrm{d}\tau \end{aligned} \tag{2.24}$$

Green's function formalism provides a direct and elegant integral solution to the acoustic problem, because the acoustic *free-field Green's function* $\mathcal{G}_0$ exists and is well known:

$$\begin{cases} \mathcal{G}_0(\mathbf{x},t;\mathbf{y},\tau) = \dfrac{\delta(t-\tau-\frac{\|\mathbf{x}-\mathbf{y}\|}{c_0})}{4\pi\|\mathbf{x}-\mathbf{y}\|} & \text{with } t \geq \tau \\ \mathcal{G}_0 = 0 \qquad \text{with } t < \tau \end{cases} \tag{2.25}$$

When free-field Green's function $\mathcal{G}_0$ employed for solving the acoustic problem in absence of walls, the expression (2.23) leads to

$$\begin{aligned} p'(\mathbf{x},t) &= \int_{-\infty}^{+\infty} \int_{\Omega} f(\mathbf{y},\tau)\mathcal{G}_0(\mathbf{x},t;\mathbf{y},\tau)\ \mathrm{d}^3\mathbf{y}\mathrm{d}\tau \\ &= \frac{1}{4\pi}\int_{\Omega_s} \frac{f(\mathbf{y},t-\frac{\|\mathbf{x}-\mathbf{y}\|}{c_0})}{\|\mathbf{x}-\mathbf{y}\|}\ \mathrm{d}^3\mathbf{y} \end{aligned} \tag{2.26}$$

where Ω_s is the source region. In aeroacoustic applications, source is generally non-compact as it results from spatially distributed, non-coherent sound production mechanisms. Therefore, eq. (2.26) is frequently applied to simulate the acoustic pressure field when a spatial distribution of sources (modeled in the forcing term f) perturbs the surroundings. In sec. 2.3.1, this formula will be employed to derive the acoustic free-field response to turbulence, whose effects are equalised to a spatial distribution of quadrupoles (it will be proven).

2.2 FREQUENCY-DOMAIN FORMULATION

Given that acoustics frequently addresses periodic signals, which can be conceptualized as a sum of harmonic functions in accordance with Fourier's theory, there may arise a curiosity in examining the acoustic field in terms of frequency. In light of this, when considering a point source placed in the origin, one can express the resultant acoustic field in the following manner according to the free-field Green's function $\mathcal{G}_0$:

$$p'(r,t) = \frac{A}{r}\cos\left[\omega\left(t - \frac{r}{c_0}\right) + \phi\right] \tag{2.27}$$

where ω is the *angular frequency* and ϕ is the *phase angle*, while $r = \|\mathbf{x}_P - \mathbf{x}_S\|$ is the distance between the source in $\mathbf{x}_S$ and the receiver in $\mathbf{x}_P$. The expression $k = \frac{\omega}{c_0}$ is referred to as *wave number* and acts as a sort of *spatial frequency*. Eq.(2.27) can be seen as the real part of the complex-valued expression in brackets:

$$p'(r,t) = \mathrm{Re}\left\{\frac{A}{r}e^{-ikr+i\phi}e^{i\omega t}\right\} = \mathrm{Re}\left\{\hat{p}'(r)e^{i\omega t}\right\} \tag{2.28}$$

Here $e^{i\omega t}$ is the phase difference due to passing of time, while $\hat{p}'(r) = \frac{A}{r}e^{-ikr+i\phi}$ is the *complex amplitude* that accounts for the wave amplitude decay with distance r and the phase difference due to ϕ and to wave propagation in space kr. In other words, $\hat{p}'(r)$ represents the *Fourier transform* for $p'(r,t)$ when the signal is a pure harmonic of frequency ω.

2.2.1 Governing equations in the frequency domain

One can think of substituting eq. (2.28) in the wave equation (2.13) to obtain

$$\mathrm{Re}\left\{\left(\frac{\omega^2}{c_0^2}\hat{p}'(\mathbf{x}) + \nabla^2\hat{p}'(\mathbf{x}) + i\omega\hat{Q}^{(m)} - \rho_0\nabla\cdot\hat{\mathbf{f}}\right)e^{i\omega t}\right\} = 0 \tag{2.29}$$

to ensure its validity, the expression in the brackets should be equaled to zero, resulting in the so-called *non-homogeneous Helmholtz equation*:

$$\nabla^2\hat{p}'(\mathbf{x},\omega) + k^2\hat{p}'(\mathbf{x},\omega) = -i\omega\hat{Q}^{(m)}(\mathbf{x},\omega) + \rho_0\nabla\cdot\hat{\mathbf{f}}(\mathbf{x},\omega) \tag{2.30}$$

where it should be noted that Fourier-transformed quantities in eq. (2.30) are, in general, functions of both $\mathbf{x}$ and ω when dealing with non-harmonic signals. The corresponding *transformed acoustic momentum equation*, firstly displayed in eq. (2.16), is

$$i\omega\hat{\mathbf{u}}'(\mathbf{x},\omega) = -\frac{1}{\rho_0}\nabla\hat{p}'(\mathbf{x},\omega) + \hat{\mathbf{f}}(\mathbf{x},\omega) \tag{2.31}$$

2.2.2 Green's function in the frequency domain

Even for the Helmholtz equation, an integral solution can be defined based on Green's formalism, just like it was done for the time-domain non-homogeneous wave equation in eq.(2.23). The Green's function for the Helmholtz equation (2.30) $\hat{\mathcal{G}}(\mathbf{x};\mathbf{y})$ is defined as the solution of:

$$\nabla^2\hat{\mathcal{G}}(\mathbf{x};\mathbf{y}) + k^2\hat{\mathcal{G}}(\mathbf{x};\mathbf{y}) = -\delta(\mathbf{x}-\mathbf{y}) \tag{2.32}$$

which is, in absence of walls, the *free-field Green's function in the frequency domain*:

$$\hat{\mathcal{G}}_0(\mathbf{x};\mathbf{y}) = \frac{e^{-ik\|\mathbf{x}-\mathbf{y}\|}}{4\pi\|\mathbf{x}-\mathbf{y}\|} \tag{2.33}$$

$\hat{\mathcal{G}}_0$ has the useful property of serving as a *transfer function for a point source* when using Fourier-transformed quantity, reducing the computation of integrals to simple multiplications. Assuming the presence of a point source $\hat{Q}$ in position $\mathbf{y}_0$, one can compute the resulting pressure field $\hat{p}(\mathbf{x},\omega)$ as

$$\hat{p}(\mathbf{x},\omega) = \int_\Omega \mathcal{G}_0(\mathbf{x};\mathbf{y})\hat{Q}(\omega)\delta(\mathbf{y}-\mathbf{y}_0)\mathrm{d}^3\mathbf{y} = \frac{\hat{Q}(\omega)}{4\pi\|\mathbf{x}-\mathbf{y}_0\|}e^{-ik\|\mathbf{x}-\mathbf{y}_0\|} \tag{2.34}$$

A fact that is a considerable advantage and will be exploited in sec. 4.2 to *formulate the acoustic imaging problem into a linear problem to be inverted.*

2.3 SOUND GENERATED AERODYNAMICALLY

The noise produced by an aerodynamic flow is physically defined as a pressure (and density, as consequence) fluctuation occurring within the flow field and travelling through it at a finite velocity denoted as c, that depends on the local properties of the fluid. Noise arises when the turbulent eddies, induced by the instability of shear flows, encounter *rapid variations in time*, e.g. due to the presence of rigid surfaces or in regions characterized by a high level of flow mixing and re-organisation of turbulent structures (ref. fig. 2.1). Typical sound production mechanisms in aerodynamics are:

- *vortex-shedding noise*, which is the result of quadrupolar sources in the wake of a bluff body scattering into the far-field, with a dipolar directivity, as a consequence of its diffraction by the body [8, 9]. A similar phenomenon can also occur at a airfoil's trailing edge;

- *trailing edge noise*, that occurs when boundary-layer disturbances scatter at a trailing edge [10];

- *leading edge noise*, that results from the interaction of a airfoil with the upstream turbulence [11];

- *jet noise*, which arises from the mixing region in a high-velocity jet flow.

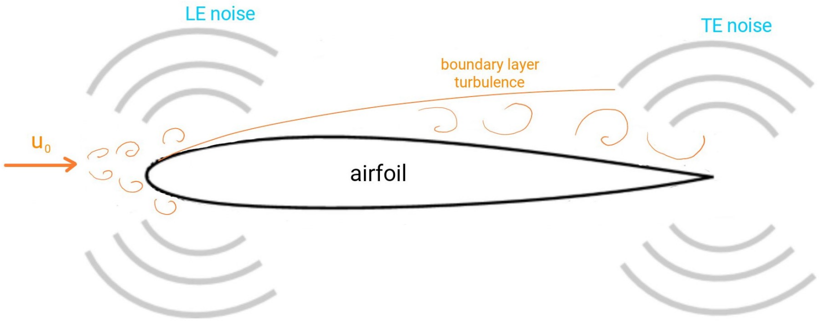

Figure 2.1: Sketch representing different contributions to airfoil noise: *leading edge noise*, *trailing edge noise* and *boundary layer noise.*

2.3.1 Aeroacoustic analogies

Sir. Lighthill [12] was the first to establish a connection between the aerodynamic flow field and the corresponding acoustic production by identifying the key aerodynamic terms and incorporating them into an exact acoustic waves equation. This initial achievement was attained through the direct manipulation of the Navier-Stokes equations without further assumptions, obtaining:

$$\frac{\partial^2 \rho'}{\partial t^2} - c_0^2 \frac{\partial^2 \rho'}{\partial x_i^2} = \frac{\partial^2 T_{ij}}{\partial x_i \partial x_j} \tag{2.35}$$

where T_{ij} stands for the *Lighthill's stress tensor*:

$$T_{ij} = \rho u_i u_j + (p' - c_0^2 \rho')\delta_{ij} - \tau_{ij} \tag{2.36}$$

Eq.(2.35), as it is analytically exact, is applicable to all fluid dynamic phenomena. The motion of the fluid is interpreted as a flow field in which fluctuations (ρ' and p', with respect to ambient quantities ρ_0 and p_0 respectively) propagate as waves, with a finite propagation velocity c_0 that matches that of the surrounding environment within the propagation zone. The Lighthill's tensor serves as an *aerodynamic forcing term* within the wave equation and implicitly characterizes all potential occurrences of sound production resulting from the existing conditions.

The equation cannot be classified as a typical linear acoustics wave equation due to its generality: the term on the right encompasses the unknown acoustic field and cannot be seen as a pure source term. Thus, it is not possible to solve the Lighthill's equation explicitly using the Green's function's formalism. The conventional methods of linear acoustics can only be employed if the term on the right can be approximately evaluated and is independent of the acoustic variables. This can only be accomplished by disregarding certain mechanisms incorporated in Lighthill's equation. Assuming:

- low Mach number: $M \ll 1$. This condition ensures that action of fluid's momentum dominates over thermal effects;
- high Reynolds number: $\mathrm{Re} \gg 1$, resulting in viscous effects being negligible.

These conditions lead to a simplified expression for the Lighthill stress tensor in eq.(2.36), known as the *Lighthill's approximation*:

$$T_{ij} \approx \rho_0 u_i u_j \tag{2.37}$$

where $\rho \approx \rho_0$ due to assumptions on Mach number. The Lighthill's tensor can now be evaluated from the flow field's solution and represents a proper forcing term for the waves equation, thereby enabling an integral solution through the Green's function:

$$\rho'(\mathbf{x},t) = \int_{-\infty}^{+\infty} \int_{\Omega} \mathcal{G}(\mathbf{x},t;\mathbf{y},\tau) \frac{\partial^2 T_{ij}}{\partial x_i \partial x_j} \ \mathrm{d}^3\mathbf{y} \ \mathrm{d}\tau \tag{2.38}$$

which represents a far-field approximated solution for the density fluctuations ρ'. In absence of walls and obstacles, a free-field Green's function $\mathcal{G}_0$ can be adopted, leading to

$$\rho'(\mathbf{x},t) = \frac{1}{c_0^2} \frac{\partial^2}{\partial x_i \partial x_j} \int_{\Omega} \frac{T_{ij}\left(\mathbf{y}, t - \frac{\|\mathbf{x}-\mathbf{y}\|}{c_0}\right)}{4\pi \|\mathbf{x}-\mathbf{y}\|} \mathrm{d}^3\mathbf{y} \tag{2.39}$$

which shows that aerodynamic noise in the free-field can be represented as the result of a spatial distribution of *quadrupolar sources*. Eq. (2.39) is valid for turbulent isentropic and incompressible ($M \ll 1$) flows in free-field conditions. Eventually, the presence of solid boundaries can be taken into account following the theory of Curle [13]. Furthermore, Ffwocs Williams and Hawkings [14] extended the aeroacoustic analogy to include arbitrary convective motion of the body.

Acoustic analogies are important tools in the *prediction of noise* of aerodynamic origin from numerical simulations (DNS/LES), as they allow the aerodynamic solution to be linked to the acoustic solution generated by it in the far-field. The advantage in their use is the fact that acoustic analogies represent an *integral analytical solution.* Therefore, once the source zone has been integrated, the resulting acoustic field can be evaluated at any point in the propagation zone, without the need to discretize the latter with a mesh. In contrast, noise prediction using DNS in the far-field, due to the fine mesh and small time-steps required, would greatly lengthen the calculation time and would undoubtedly only be possible on particularly well-equipped computers.

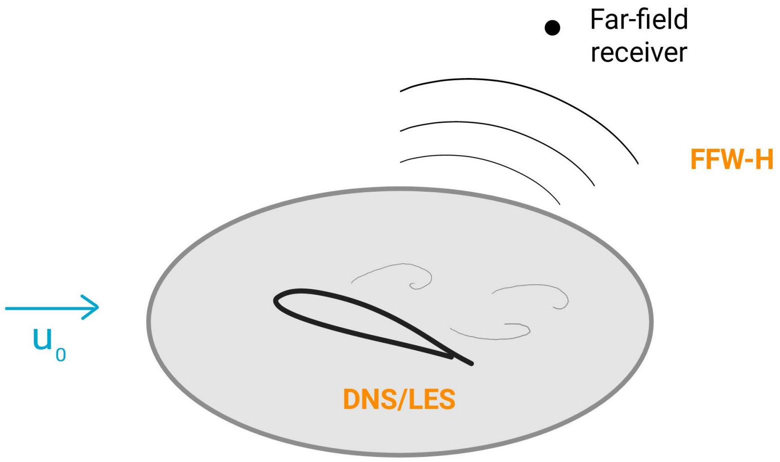

Figure 2.2: Numerical noise prediction using the FFW-H acoustic analogy. The gray region is discretized with a fine mesh and DNS or LES are applied so that the aerodynamic field generating noise is determined. On the boundary surface, fictitious acoustic sources are collected that, according to the analogy, produce the same far-field acoustic fluctuations as those produced by aerodynamics within the region. These sources are then propagated in accordance with the *convected wave equation*. In this way, the effects of the presence of *moving solid bodies* within the grey region are taken into account.

This becomes even more evident when measurements are collected for the purpose of *source imaging*. In fact, these require the evaluation of the acoustic field at only *a few points*, i.e. the microphones. Therefore, the use of acoustic analogies is definitely the most feasible approach.

Chapter3

FUNDAMENTALS OF BEAMFORMING

This chapter will investigate the basic principles behind the beamforming analysis, which relies on far-field microphone arrays measurements with the purpose to resolve the acoustic sources distribution associated with the aerodynamic flow field. To accomplish this task, Glegg and Devenport's manual [15] will be employed as theoretical reference.

After a brief introduction on the *phased arrays* technology in sec. 3.1, the ideas behind *array processing* will be explained in sec. 3.2. Then, the complexities occurring in beamforming when applied to aeroacoustics will be elucidated in sec. 3.3.

3.1 PHASED ARRAYS

In the realm of aeroacoustic measurements, whether conducted within a wind tunnel or as part of a numerical simulation, the researcher may have the desire to ascertain not only the overall levels of noise but also the precise location of the sound sources within the motion field and their interrelated intensity. Specifically, the aim is to simultaneously resolve and characterize all acoustic sources within the motion field, taking into account their intensity, emission frequency, and spatial positioning. As an illustrative example, when examining an airfoil, one may want to separate the sources situated at the leading edge, which give rise to what is known as *leading edge noise*, and those found at the trailing edge, responsible for the occurrence of *trailing edge noise* (ref. fig. 4.1). In addition, aeroacoustic sources are often not compact and isolated but sparse and spatially distributed, causing several difficulties and uncertainties in the reconstruction due to possible interference.

To accomplish this objective, the utilization of *phased arrays* becomes necessary. By employing a technique known as *beamforming* which involves the manipulation of signals captured in the far field by a set of microphones housed within a suitably shaped support structure, one can effectively chart the distribution of acoustic sources. This mapping process

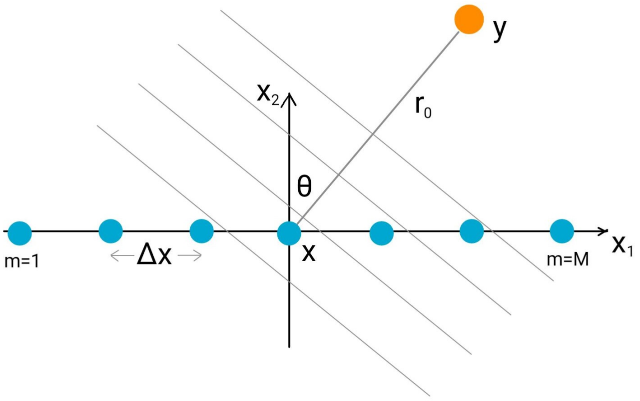

Figure 3.1: Line array of M microphones receiving acoustic waves from a far-field source located in $\mathbf{y}$

relies on a *signal propagation model* which is dependent upon a variety of factors, including environmental conditions, the presence of obstacles within the field, the particular type of sources that are to be included in the analysis, and, in the context of aeroacoustic applications, the convection influenced by the mean flow velocity.

3.2 Array processing for Beamforming

The underlying concept of *phased array* is founded upon the observation that every single acoustic ray follows a different path once emitted by the source. This fact is due to a finite propagation velocity (namely, the speed of sound c) and results into a phase difference in the recorded signals between the microphones in the array, which makes the source's position become detectable.

In order to gain comprehension about phased arrays, the most elementary scenario which involves a isolated point source situated in the far field will be examined. It will be demonstrated how a linear array of microphones is capable of ascertaining both the position and intensity of said source, and important attributes of the employed array, such as *spatial resolution* and *aliasing*, will be uncovered. Moreover, the *delay and sum* principle will be introduced, which allows for the virtual manipulation of the beam direction and serves as the cornerstone for all beamforming signal processing approaches. Ultimately, the primary challenges associated with this methodology will be demonstrated, emphasizing its relevance in aeroacoustic applications.

3.2.1 Single source in far field

The expression for the far-field acoustic pressure induced by an harmonically pulsing source, in the frequency domain, is given by

$$\hat{p}(\mathbf{x}) = -\frac{i\omega\rho_0 a e^{ikr}}{4\pi r} \tag{3.1}$$

where a represents the the magnitude of the fictitious volume rate and $r = \|\mathbf{x} - \mathbf{y}\|$ is the distance between the source at $\mathbf{y}$ and the microphone at $\mathbf{x}$, with reference to fig. 3.1. Since the source is located in the far field, the following approximation can be adopted for the distance:

$$r = \left\| r_0 - \frac{\mathbf{x} \cdot \mathbf{y}}{r_0} \right\| \tag{3.2}$$

with $r_0 = \|\mathbf{y}\|$ is the distance of the source from the center of the array, placed in $\mathbf{x} = (0, 0, 0)$. Eq. (3.2) is equivalent to assuming wavefronts to be planar. Each microphone in the array is located at $\mathbf{x}_m = ((m-1)\Delta x - L/2, 0, 0)$, with $L = (M-1)\Delta x$, resulting in eq. (3.2) to be specialized for every m microphone in the M-microphones linear array. Since the probes are placed along the x_1 axis:

$$r^{(m)} = r_0 - x_1^{(m)} \sin\theta \tag{3.3}$$

where θ is the angle between the source and the x_2 axis. In eq. (3.3), the latter term is responsible for the phase difference between the M recorded signals emitted by the source in $\mathbf{y}$.

It is now possible to write the pressure at each transducer:

$$\hat{p}(\mathbf{x}_m) = \left(\frac{-i\omega\rho_0 a e^{ikr_0}}{4\pi r_0} \right) e^{-ik((m-1)\Delta x - L/2)\sin\theta} \tag{3.4}$$

As a consequence, the array output can be computed as average of the M Fourier-transformed recorded signals as displayed below:

$$\hat{p}_t = \frac{1}{M}\sum_{m=1}^{M} \hat{p}(\mathbf{x}_m) = \frac{-i\omega\rho_0 a e^{ikr_0 + \frac{i}{2}kL\sin\theta}}{4\pi r_0} \left(\frac{1}{M}\sum_{m=1}^{M} e^{-ik(m-1)\Delta x \sin\theta} \right) \tag{3.5}$$

which is a geometric series that can be summed to give

$$\hat{p}_t = \frac{-i\omega\rho_0 a e^{ikr_0}}{4\pi r_0} \Phi(kL\sin\theta) \tag{3.6}$$

with

$$\Phi(kL\sin\theta) = \frac{\sin\left(\frac{1}{2}kM\Delta x \sin\theta\right)}{M\sin\left(\frac{1}{2}k\Delta x\sin\theta\right)} \tag{3.7}$$

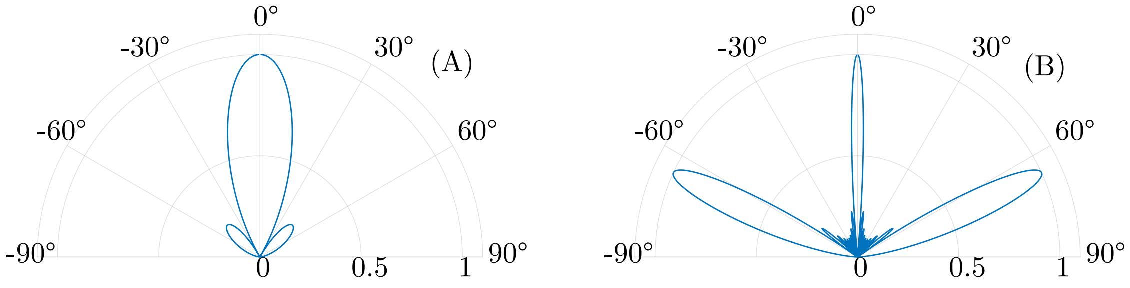

(a) $kL = 11$, $M = 10$

(b) $kL = 62$, $M = 10$

Figure 3.2: **(a)**: Array sensitivity Φ for different values of kL.

The Φ function, shown in fig. 3.2, is responsible for the modulation of the array output $\hat{p}_t$, depending on the source angular position θ with respect to the array's normal direction. If the source is in front of the array ($\theta = 0°$), all the microphones record the same in-phase signal and Φ reaches its maximum value of 1. If θ is increased, signals start to become out-of-phase and $\Phi < 1$, until it reaches the value of 0 for some angles and starts increasing again.

3.2.2 Spatial aliasing and resolution

Referring to fig. 3.2.b, there is a fundamental ambiguity in identifying the source position: if the array sensitivity has multiple *beams*, there can be multiple angles where the array output reaches a maximum, leading to the problem of *spatial aliasing* that results in uncertainty regarding the precise location of the source in a practical situation. Spatial aliasing can be avoided by ensuring that $\|\frac{1}{2}k\Delta x \sin\theta\| < \frac{\pi}{2}$, a condition that can be satisfied by imposing $\Delta x < \lambda/2$ (λ being the acoustic wavelength), which represents a geometrical constraint for the microphones array.

The *spatial resolution* of the array is usually associated to the angular or linear width of the central beam over which the array output drops to 3 dB below its maximum value. This corresponds to $\Phi = 0{,}707$, that occurs approximately when $kM\Delta x \sin\theta = 2.8$. In order to fulfill the conditions set forth by spatial aliasing and spatial resolution, it is imperative to employ arrays of considerable magnitude and minimal spacing between the transducers, consequently necessitating a substantial quantity of transducers.

In any circumstance, the wavenumber k assumes a pivotal role in varying the spatial response of the array so that, under the condition of other variables being equivalent:

- for small k, the strength and number of *sidelobes* as well as the spatial resolution diminish, and the central beam gets wider;

- for greater k, the strength and quantity of *sidelobes* and the spatial resolution increase, yet you can attain a multitude of local maxima in acoustic maps. Furthermore, the possibility of encountering the issue of spatial aliasing remains.

The aforementioned factors ensure that the performance of the beamformer in mapping the acoustic field accurately is greatly contingent upon the configuration of the array and the frequency range to be examined.

3.2.3 Array design

To address the challenges arising from spatial aliasing, particularly at high frequencies, and the need for high resolution at low frequencies, it becomes essential to abandon the idea of an array of equally spaced microphones.

In essence, one can contemplate an arrangement of microphones with unequally spacing, incorporating both closely positioned microphones to mitigate aliasing issues and larger apertures to enhance spatial resolution at lower frequencies, all while maintaining a reasonable number of microphones. This objective can be achieved by employing logarithmically spaced microphones.

In reality, attempts are made to capture the acoustics of two-dimensional or three-dimensional areas, requiring the use of a spatial distribution of microphones. Common designs include circular or rectangular arrays, in which the microphones are embedded in a planar arrangement. These arrays can be employed individually or in conjunction with arrays of the same type placed on a normal plane, particularly in the context of three-dimensional beamforming. Similarly to linear arrays, these configurations also face the challenges of aliasing and resolution, which depend on the array's extension and spacing of the transducers. However, one notable difference is that the number of microphones can rapidly increase in these setups, resulting in higher costs. An optimal compromise is offered by planar spiral arrays [16], that arrange the transducers as follows:

$$r_m = r_s e^{h\theta_m} \tag{3.8}$$

where r_m and θ_m are rispectively the radial and the angular position of the m-microphone and r_s is the inner transducer's radial position, while h is a scaling factor.

3.2.4 Beam steering and Delay&Sum principle

Ideally, one could physically steer the microphone array in pursuit of determining the direction from which the acoustic waves emit. Although this approach is theoretically feasible, it lacks the necessary precision. An alternative method involves virtually steering the array to specific points within the domain to examine potential sources. This is achieved by time-shifting the signals collected by the microphones, while taking into consideration the phase difference $\phi_m = kr^{(m)}$ that accumulates along the path between the hypothetical source in

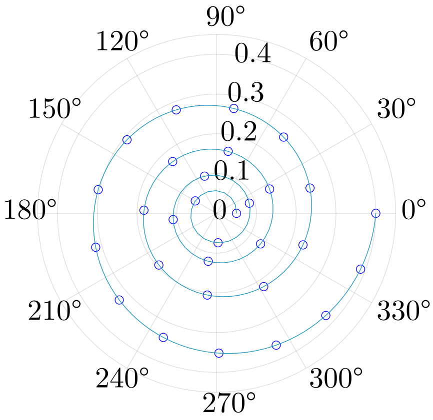

Figure 3.3: Example of spiral array with equally-spaced tranducers along the spiral: $r_{\max} = 0{,}4$m, $r_s = 0{,}05$m e $h = 0{,}08$.

the interrogation area and each individual microphone. If the average of the shifted signals produces a discernible signal characterized by a non-zero variance $\overline{p_t^2}$, it indicates the presence of an acoustic intensity source in the interrogation zone. Referred to as the *delay and sum* principle, this concept serves as the basis for various acoustic beamforming algorithms, either directly or indirectly. In this case, the array's output when focusing on the hypothetical source s is calculated as:

$$\hat{p}_{t,s} = \frac{1}{M}\sum_{m=1}^{M} \hat{p}(\mathbf{x}_m)e^{i\phi_{m,s}} = \frac{-i\omega\rho_0 a e^{ikr_0}}{4\pi r_0}\,\Phi(kL(\sin\theta - \sin\theta_s)) \tag{3.9}$$

where the m-th microphone's phase shift $\phi_{m,s}$ for the linear array case depicted in sec. 3.2.1 is

$$\phi_m = k\left((m-1)\Delta x - \frac{1}{2}L\right)\sin\theta_s \tag{3.10}$$

In eq. 3.10, the value of θ_s is driven by the choice of the interrogation area when beam-steering. The signal obtained results to be identical to the array output when the array points toward the source. The introduced methodology, when applied to a grid of potential sources obtained by discretizing the acoustic field for analysis, enables the determination of source magnitudes at each calculation point.

3.3 Beamforming in Aeroacoustics

When acoustic imaging analyses have to be carried out in aeroacoustic problems, especially when based on wind tunnel measurements, additional criticalities to those normally present (seen in sec. 3.2.2) come to light. First, it must be said that aerodynamic sources are *rarely monopoles*, as this type of source represents the effect of moving membranes capable of generating a fictitious variation in flow rate over time. More often, aeroacoustic sources are idealised as *dipoles* (representing the response of rigid surfaces to pressure fluctuations over time [13]) and quadrupoles, a concept through which Lighthill (ref. sec. 2.3.1) modelled far-field pressure waves given by turbulent fluctuations, shear stresses and entropy variations. This complicates things modestly, both because it becomes necessary to use arrays capable of capturing the directionality of these multipolar sources while still fulfilling the requirements of spatial aliasing and resolution, and because imaging these sources implies modelling acoustic propagation that is no longer omnidirectional, but takes into account the directionality of the sources. In the present work, this was done for dipolar sources, which were included in the beamforming analysis by implementing a transfer function that adequately takes into account every possible dipole freely oriented in space. In the case of quadripolar sources, however, the complexity of the acoustic field they generate and the countless existing combinations make it impossible to go down this route.

Nonetheless, the presence of bodies within the domain can also cause fictitious sources to appear in the solution, resulting from the reflection of acoustic waves on them, and makes it theoretically necessary to adopt a propagation model that takes this into account, for example by using tailored Green's function, or by placing sources within the domain to simulate the effect that the presence of the body has in the acoustic field [17].

Another thing that complicates beamforming in the aeroacoustic field is the fact that the aerodynamically generated noise is referable to a *spatial distribution of multiple sources* within the domain of interest, which may interfere with each other and do not make it possible to apply conventional methods satisfactorily, as these are based on the assumption that the interrogation region contains the only source within the domain. In this work, this need is met by introducing the *Generalized Inverse Beamforming* (GIBF), belonging to the class of *inverse methods*, capable of *resolving the acoustic field simultaneously*, thus modelling the overall effect of the sources and inherently taking into account the interference that may occur. Furthermore, the shear layer that envelops aerodynamic models, together with the background noise that inevitably plagues experimental wind tunnel measurements, make it necessary to use *de-noising techniques* to avoid the generation of physically irrelevant, or nonsensical, solutions.

Finally, unlike traditional beamforming, in aeroacoustics beamforming deals with sources transported by the average flow velocity, which causes a *shift in the source image* in the reconstruction with respect to its actual position. This phenomenon is exacerbated in analyses based on wind tunnel measurements, where the presence of a *shear layer* between the acoustic production region and the microphone array (for obvious reasons) causes the refraction of travelling acoustic waves. These issues represent additional complexities that will be taken into account in the sections 4.5,4.6.

Chapter4

METHODOLOGY

In this chapter, the author presents the methodology behind the development of a beamforming tool suitable for aeroacoustics based on a inverse technique, namely the *Generalized Inverse Beamforming* (GIBF) introduced by Suzuki [7], taking as a starting point the work of Zamponi [18], who developed the initial codebase and enhanced the algorithm with significant considerations on the inverse problem's regularization strategy [18]. After an introduction on inverse methods and the necessity behind their implementation in sec. 4.1, the source imaging problem will be formulated as a linear system to be inverted (sec. 4.2). Then, the eigendecomposition of the *cross-spectral matrix*, allowing to only consider the most energetic eigenmodes and separate different sound production mechanisms, will be presented in sec. 4.3. In sec. 4.4, a strategy to extend the tool's capabilities and permit dipole detection is explained and applied. Futhermore, corrections for the shifting effect given by flow velocity convection and the presence of shear layers in open-jet wind tunnel measurements are accounted (sec. 4.5,4.6). In sec. 4.7, the *Iterative Re-weigthed Least Squares* (IRLS) inversion algorithm will be elucidated and an extension to 3D domains will be explored in sec. 4.8.

4.1 INTRODUCTION TO INVERSE METHODS

In sec. 3.2.4, it has been demonstrated how the array signals can be processed to acquire data regarding the existence and strength of an acoustic source within a confined area of a given discretized domain. Approaches like the one mentioned are built upon the underlying assumption that the region under investigation may potentially contain the sole source within the whole domain. This assumption poses a significant constraint in situations where this fundamental hypothesis fails, as is the case in *aeroacoustic analysis*, a field known for its complexities and challenges, as expounded upon in sec. 3.3, foremost among them, the existence of space-distributed coherent and incoherent sources, e.g. with reference to fig.

4.1, *airfoil noise* results from different contributions, namely *leading edge noise*, *trailing edge noise* and *boundary layer noise* (see sec. 2.3). The necessity to overcome the limitations highlighted gives rise to a new category of acoustic imaging methods that are suitable for dealing with these more complex scenarios.

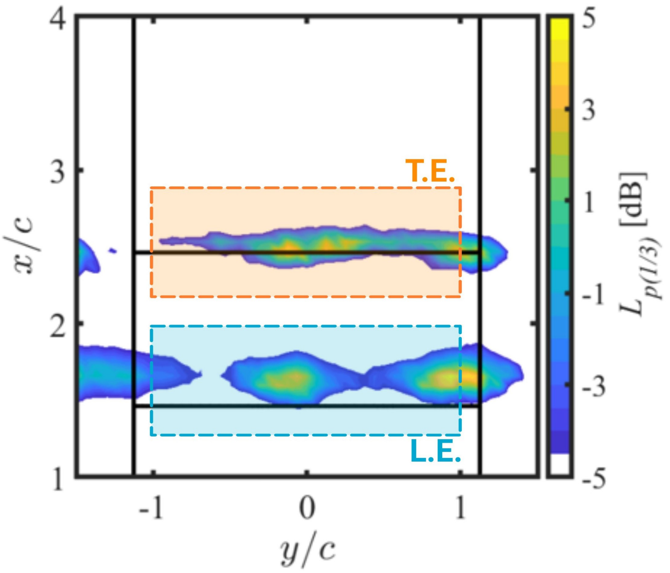

Figure 4.1: Sound map of a airfoil generated with GIBF *tool* showing the sources responsible for leading edge noise and trailing edge noise, that can be integrated separately to quantify their relative contribution to emitted noise.

Included in this category are the *inverse methods*, which, despite sharing the same acoustic propagation model between the source and the receiver as the direct methods, possess the advantage of *simultaneously resolving the entire acoustic field.* As a result, they are able to take into consideration the acoustic patterns that can be formed as a result of the presence of multiple sources, whether they are correlated or uncorrelated, or due to their phase shift, unveiling the possibility of accurately localize and quantify aeroacoustic sources and even improving the source map resolution by *promoting sparsity* in the reconstruction process. Among these, the *Generalized Inverse Beamforming* proposed by Suzuki [7] represents a robust and feasible method that proved significant reliability in source imaging. Therefore, this technique was adopted as the theoretical basis for the implementation that is carried out in the present work.

However, these advantages come with quite a few *complexities.* The fact that inverse methods have the capability to simultaneously solve all potential sources often leads to the inversion of an *underdetermined linear problem*, the solution of which is typically not straightforward and *heavily reliant on the measurement noise.* It is imperative to employ appropriate mathematical techniques to safeguard against this. Furthermore, there is also a growing demand for *computational resources*, including increased calculation time for solving *large linear*

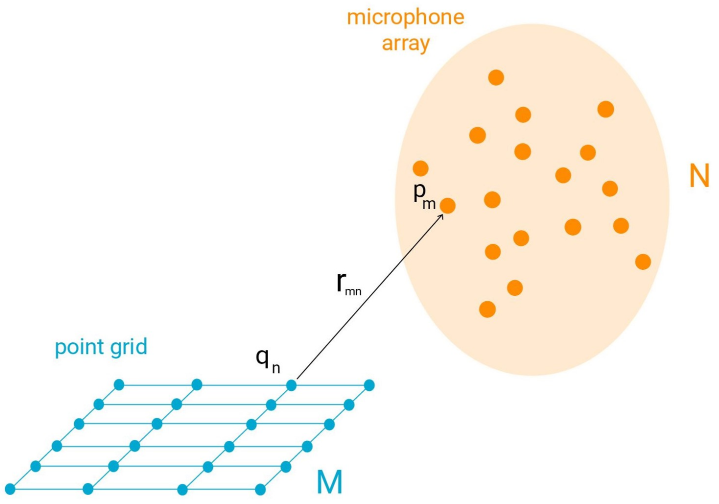

Figure 4.2: Scheme of the propagation between the n-th grid point source q_n to the m-th microphone.

problems, thereby emphasizing the importance of providing adequate hardware.

4.2 Inverse problem formulation

Discretizing the spatial domain in which acoustic sources can be located can be done by using a two-dimensional or three-dimensional grid of N points to represent their position. By knowing the spatial position of the M microphones that receive the signals, the acoustic pressure (from now on referred to as p for clarity) at the microphone m resulting from the the monopolar point source n (other possibilities will be explored in sec. 4.4) can be expressed, in the frequency domain, as:

$$\hat{p}_{mn} = A_{mn}\hat{q}_n \tag{4.1}$$

in which $\hat{p}_{mn} \equiv \hat{p}(\mathbf{x}_m; \mathbf{x}_n)$ represents the acoustic pressure at the m-th microphone caused by the n-th source (refer to fig. 4.2), $\hat{q}_n$ is the Fourier-transformed source strength of the monopole source placed in grid point $\mathbf{x}_n$ having units Pa m and A_{mn} is the *transfer function* between the n-th source and the m-th microphone and having expression:

$$A_{mn} = \frac{e^{-ik\|\mathbf{r}_{mn}\|}}{4\pi\|\mathbf{r}_{mn}\|} \tag{4.2}$$

where $\mathbf{r}_{mn} = \mathbf{x}_m - \mathbf{x}_n$, $n = 1, ..., N$ and $m = 1, ..., M$. Eq. (4.1) can be derived from eq. (2.34) when dealing with a monopolar point source. In fact, one should easily note that, for a monopole-like propagation model, A_{mn} corresponds to the free-field Green's function $\mathcal{G}_0(\mathbf{x}_m; \mathbf{x}_n)$, here adopted for the sake of simplicity, although a tailored Green's function can be applied as well in reverberating environments.

The inverse formulation of the direct source-microphone propagation problem is grounded in the modeling of the m-th microphone pressure $\hat{p}_m$ generated by the *superposition of signals from all sources at each grid point.*

$$\hat{p}_m = \sum_{n=1}^{N} \hat{p}_{mn} = \sum_{n=1}^{N} A_{mn}\hat{q}_n \tag{4.3}$$

It is summarised in the following linear system:

$$\hat{\mathbf{p}} = \mathbf{A} \cdot \hat{\mathbf{q}} \tag{4.4}$$

where $\hat{\mathbf{p}} = (\hat{p}_1, ..., \hat{p}_M)^{\mathrm{T}}$ and $\hat{\mathbf{q}} = (\hat{q}_1, ..., \hat{p}_N)^{\mathrm{T}}$. In most applications, for cost reasons, the number of microphones M is considerably little compared to the number of grid points N, leading the problem to be *underdetermined*, with a plurality of solutions existing within which to select the physically most appropriate one. As it is by far the most frequent and realistic, only the *underdetermined case* will be handled within the discussion, although the *overdetermined case*, even if of minor importance, also exists. The resolution of such problems necessitates giving a special care to *measurement noise*, as they demonstrate an extreme sensibility to it. Consequently, when subjected to even a low level of noise, the obtained solution may diverge significantly from the optimal one, occasionally resulting in solutions devoid of physical meaning. For these reasons, sometimes the adoption of *de-noising techniques* becomes necessary.

In addition, because $\mathbf{A}$ matrix is not generally square having dimensions $M \times N$, it is not *invertible.* Hence the solution is to be found via *direct or iterative methods*, depending on the characteristics one seeks to promote in the solution to be selected. Section 4.7 will be dedicated to this aspect, where a $\mathcal{L}_1$ minimum-norm solution to eq. (4.4) will be sought via an iterative method, namely the IRLS method.

4.3 Cross Spectral Matrix eigen-decomposition

In eq. (4.4), pressure $\hat{\mathbf{p}}$ results from the superposition of the whole set of sources that contribute to the exact reconstruction relatively to the chosen propagation model (it is not exact in the broadest sense since the source reconstruction is subjected to discretization and to the imposed source model and doesn't necessarily reflect the physics behind the sound production mechanism).

To shed light on the different coherent source distributions that constitute specific sound production mechanisms (e.g. *leading edge noise* and *trailing edge noise*) and take into account only the most relevant ones in source reconstruction, the microphones' signals are firstly combined in the *cross-spectral matrix* $\mathbf{\Gamma}$, generated by averaging the Fourier-transformed sample blocks (in Welch's method) over time:

$$\mathbf{\Gamma} = \overline{\hat{\mathbf{p}}\hat{\mathbf{p}}^{\mathrm{H}}} \tag{4.5}$$

where $\hat{\mathbf{p}}$ represents the vector of the Fourier-transformed pressure signals and $\mathbf{\Gamma}$, when evaluated for a certain frequency ω^*, is a complex-valued non-negative definite and Hermitian $M \times M$ matrix. Because of its mathematical properties, a *eigendecomposition* can be performed:

$$\mathbf{\Gamma}_{\omega^*} = \mathbf{U}\mathbf{\Lambda}\mathbf{U}^{\mathrm{H}} \tag{4.6}$$

in which $\mathbf{U}$ is a unitary matrix containing orthonormal eigenvectors on its columns, $\mathbf{\Lambda}$ is a diagonal matrix containing eigenvalues λ_i, and $\mathbf{U}^{\mathrm{H}}$ is the complex conjugate transpose of $\mathbf{U}$. This procedure makes it possible to *solve different coherent source distributions separately*, since their contribution to recorded noise is summarised by their respective eigenmodes, representing *different coherent sound production mechanisms*:

$$\boldsymbol{\nu_i} = \sqrt{\lambda_i}\mathbf{u}_i \tag{4.7}$$

where $\boldsymbol{\nu_i}$ is the i-th eigenmode, $\mathbf{u}_i$ is the i-th column vector of $\mathbf{U}$ and λ_i is the corresponding eigenvalue. Normally, the eigendecomposition of the cross-spectral matrix is known to showcase only the most important contributions to the pressure recorded by the microphone array, represented by the greatest eigenvalues, while eigenvalues associated with *non-coherent random signal noise* are generally small in magnitude. Hence, the problem can be reformulated as:

$$\boldsymbol{\nu}_i = \mathbf{A} \cdot \hat{\mathbf{q}}_i \tag{4.8}$$

where $\hat{\mathbf{q}}_i$ is the vector representing the *complex amplitudes of coherent sources* (at each of the N grid points) designed to produce at the M microphones the pressure defined by the i-th eigenmode $\boldsymbol{\nu}_i$ via the transfer function $\mathbf{A}$. Once the solution to eq. (4.8) is known, because $\hat{\mathbf{q}}_i$ is a distribution of coherent sources representing a certain sound production mechanism, the *overall source amplitude* $\hat{Q}_i$ due to the latter is integrated by straight-summing its elements:

$$\hat{Q}_i = \sum_{n=1}^{N} \hat{q}_{i,n} \tag{4.9}$$

Regarding the *total source amplitude* Q_{tot} associated with a frequency, the squared-sum is compulsory because the *different eigenmodes result to be incoherent*:

$$Q_{\mathrm{tot}}^2 = \sum_i |\hat{Q}_i|^2 \tag{4.10}$$

where subscript i indicates the set of eigenmodes considered.

4.3.1 Eigenmodes selection

When eigendecomposition is applied to the CSM, each resulting eigenmode is composed of *coherent sources*, thus attributable to *a common mechanism of acoustic production*. This raises a question regarding which eigenmodes to consider in the beamforming analysis once the CSM is decomposed. The problem stated in eq. (4.8) is to be solved for every eigenmode one assumes to be significant. One possible approach involves comparing the magnitudes of the eigenvalues, as it is understood that these are associated with the acoustic energy of the eigenmodes. By computing the eigenvalue $\lambda_{\max}$ with the maximum magnitude, one feasible approach [19] is to only consider eigenmodes whose relative eigenvalues $\lambda_i > 0.1\ \lambda_{\max}$. This facilitates the automation of the process when automated computation is required.

4.3.2 Noise in measurements

The noise present in measurements can lead to inaccuracies in reconstructing the acoustic field, particularly when employing inverse methods, often associated with the inversion of underdetermined linear systems (as mentioned in sec. 4.2). The background and the electronic instruments, to mention the most common, introduce noise in the microphone-recorded pressure measurements and thus could make it necessary to apply de-noising techniques to the resulting CSM in eq. (4.5). Even though the noise can be high, generally it appears to be uncorrelated from microphone to microphone, hence affecting only the diagonal elements of the matrix. An effective approach in de-noising is represented by the CSM's *diagonal removal* [15], a procedure which is capable of eliminating the instrumentation noise. While the diagonal removal does not affect the source localization, it can undermine the source amplitude reconstruction due to the less data available. However, this problem seems not to be significant when the number of probes is large. This technique, even if rudimentary, provides satisfactory results. More precise techiques are also available in literature [20, 21].

4.4 MULTIPOLE DETECTION ALGORITHM

The discussion in sec. 4.2 focused on the beamforming of monopolar sources. Nonetheless, monopolar sources are associated with flow rate fluctuations, such as those resulting from membrane movements. Conversely, in *aeroacoustic scenarios*, multipolar sources predominate, displaying specific directivity and being linked to fluid interactions with *rigid surfaces* (*dipoles*) or the rearrangement of *turbulent eddies* (*quadrupoles*).

The expression provided by the eq. (4.4) is general and allows for various selections of matrix **A**, representing source-receiver propagation. Therefore, just as the GIBF algorithm is inherently constructed, there is also the possibility to configure the matrix for modeling *dipolar source-microphone propagation.* Liu et al. [22] formulated a transfer function for point dipole sources that exhibits a monopolar decay with distance but also accounts for directionality:

$$A_{mn} = \frac{e^{-ik\mathbf{r}_{mn}}}{4\pi\|\mathbf{r}_{mn}\|}\left[\boldsymbol{\zeta}\cdot\frac{\mathbf{r}_{mn}}{\|\mathbf{r}_{mn}\|}\right] \tag{4.11}$$

where $\mathbf{r}_{mn} = \mathbf{x}_m - \mathbf{x}_n$ and $\boldsymbol{\zeta}$ is a unitary vector representing the dipole's axis. Since the acoustic field resulting from a dipole is characterized by a well-defined directivity determined by its axis, unlike monopole, to guarantee a physically significant source reconstruction *three orthogonal dipoles*, x-oriented, y-oriented and z-oriented[1], are simultaneously considered *overlapped at each grid point.* In addition, it must be bear in mind that formulation in eq. (4.11) represents a far-field approximation and should be adopted with care when dealing with real-world problems.

In multipole detection, specifically when aiming to detect dipoles, $\mathbf{A}$ has dimensions $M \times (3N)$ and is composed of three sub-matrices $\mathbf{A}_x$, $\mathbf{A}_y$ and $\mathbf{A}_z$, each of them representing the acoustic field of a specific axis-aligned dipole. Consequently, also the source-strength vector $\hat{\mathbf{q}}$ will contain $3N$ elements organized in three sub-vectors $\hat{\mathbf{q}}_x$, $\hat{\mathbf{q}}_y$ and $\hat{\mathbf{q}}_z$ representing the strength of the above-mentioned dipoles at each grid point n. In symbols:

$$\hat{\mathbf{p}} = \begin{bmatrix}\mathbf{A}_x & \mathbf{A}_y & \mathbf{A}_z\end{bmatrix}\cdot\begin{bmatrix}\hat{\mathbf{q}}_x \\ \hat{\mathbf{q}}_y \\ \hat{\mathbf{q}}_z\end{bmatrix} \tag{4.12}$$

Considering dipoles oriented in all 3 directions ensures that the acoustic energy detected by the microphones is sensibly distributed among the sources most likely to have generated that pressure field.

Finally, it is important to remember that the possibility of mapping the acoustic field with dipolar sources is strongly linked to the ability of the array employed to capture the directionality of dipoles in space, and the phase difference between diametrically opposed receivers. For this reason, *multi-dimensional arrays*, such as bi-planar or spherical arrays, will be employed in multipole detection.

4.5 FORMULATION FOR CONVECTED SOURCES

The transfer function for the monopole point source in eq. (4.2) is based on the free-field Green's function in eq. (2.33) that results from the wave equation presented in eq. (2.13). In aeroacoustic applications, acoustic waves are observed to propagate through a moving fluid instead of a still one, with a non-negligible velocity $\mathbf{u}_0$. As a result, the standard wave equation may not be applicable for describing wave propagation accurately. Consequently,

---

[1] This is not peremptory. Other choices are possible for the dipoles' orientations, provided that $\{\boldsymbol{\zeta}_1, \boldsymbol{\zeta}_2, \boldsymbol{\zeta}_3\}$ constitute a basis for $\mathbb{R}^3$

one can consider incorporating the effect of fluid motion by introducing an average velocity into the equation, i.e. assuming as model the *convected wave equation* in eq. (2.12), which can be derived from the LEE (eq. (2.10)). This approach leads to the development of a *convected transfer function* A_{mn} [23]:

$$A_{mn} = \frac{e^{-ikc_0 \Delta t_e}}{4\pi\sqrt{(\mathbf{M}\cdot\mathbf{r}_{mn})^2 + \beta^2\|\mathbf{r}_{mn}\|^2}} \tag{4.13}$$

where $\mathbf{M} = \mathbf{u}_0/c_0$ is the Mach number of the uniform flow, $\beta = (1 - \|\mathbf{M}\|^2)^{\frac{1}{2}}$ (only in this context) and Δt_e is the *emission time delay*, defined as

$$\Delta t_e = \frac{1}{c\beta^2}\left(-\mathbf{M}\cdot\mathbf{r}_{mn} + \sqrt{(\mathbf{M}\cdot\mathbf{r}_{mn})^2 + \beta^2\|\mathbf{r}_{mn}\|^2}\right) \tag{4.14}$$

Concerning the dipole-beamforming, starting from eq. (4.11) a similar approach is here proposed, leading to the following formulation:

$$A_{mn,\zeta} = \frac{e^{-ikc_0 \Delta t_e}}{4\pi\sqrt{(\mathbf{M}\cdot\mathbf{r}_{mn})^2 + \beta^2\|\mathbf{r}_{mn}\|^2}}\left[\boldsymbol{\zeta}\cdot\frac{\mathbf{r}_{mn}}{\|\mathbf{r}_{mn}\|}\right] \tag{4.15}$$

that is based on the observation that dipole propagation has been modeled with a monopolar amplitude decay. Eq. (4.15) is not rigorous, as it does not derive from eq. (2.12), but rather responds to practical needs. This is why it is expected to work well in localization, but not in the quantification of dipoles.

4.6 Shear layer correction for wind tunnel measurements

When conducting measurements using arrays of microphones within *open-jet wind tunnels*, it is deemed advisable to position the microphones external to the airflow, specifically within the controlled laboratory setting. This spatial arrangement introduces a shear layer between the acoustic source region and the microphones, leading to *refraction of acoustic waves* as they propagate towards the microphone array. Not considering this refraction phenomenon results in an erroneous spatial shift of the sound sources in the acoustic mappings. Sijtsma [23] suggested a solution that involves a correction for the Mach number:

$$\mathbf{M}_{\text{corr}} = \mathbf{M}\,\frac{z_n - z_{\text{SL}}}{z_n - z_m} \tag{4.16}$$

where z_{SL} is the mean shear layer distance from the grid and $\mathbf{M}_{\text{corr}}$ is intended to be used in eq. (4.13)(4.15) in place of $\mathbf{M}$. Although finer choices are available in literature [24], the equation gives satisfactory results for Mach numbers less than 0,25 and for angles between shear layer and acoustic waves greater than 45°.

4.7 ITERATIVE RE-WEIGHTED LEAST SQUARES ALGORITHM

Because, for cost reasonability, the number of microphones M is generally lower than the number of grid point N, the linear problem stated in eq. (4.8) is generally underdetermined and ill-posed in the sense of Hadamard. Therefore it is not directly invertible but a minimum-norm solution $\hat{\mathbf{q}}_i$ is to be selected among an infinite number of solutions satisfying the equation.

In an aeroacoustic problem, the presence of acoustic sources is confined to specific regions within the domain, which correspond to solid surfaces or regions where there is significant mixing and rearrangement of turbulent eddies (a more detailed explanation is given in sec. 2.3,3.3). Consequently, it is desirable to opt for an $\mathcal{L}^1$ minimum-norm solution, as these solutions are designed to concentrate the energy of the solution in a small number of grid points. This ensures that the majority of the sources have zero amplitude, thereby preserving the fundamental physics of the problem. Conversely, the minimization of the $\mathcal{L}^2$ norm tends to favor solutions that exhibit a more evenly distributed energy among the grid points, assigning acoustic sources even in areas where they do not naturally occur.

4.7.1 $\mathcal{L}^2$ minimum-norm solution

Following these considerations, one would like to find the $\mathcal{L}^1$ minimum-norm solution $\hat{\mathbf{q}}^{(1)}$ (where subscript i is omitted for simplicity) that solves equation (4.8). The problem can be tackled only iteratively exploiting, for every eigenmode, the $\mathcal{L}^2$ minimum-norm solution $\hat{\mathbf{q}}^{(2)}$ to the equation as a starting point and thus considering the *regularized problem* stated below:

$$\hat{\mathbf{q}}^{(2)} = \operatorname{argmin}\left\{\mu_R^2\|\hat{\mathbf{q}}\|_2^2 + \|\boldsymbol{\nu} - \mathbf{A}\hat{\mathbf{q}}\|_2^2\right\} \tag{4.17}$$

where μ_R represents the Tikhonov's regularization factor. The addition of $\mu_R^2\|\hat{\mathbf{q}}\|_2^2$ to the squared residual $\|\boldsymbol{\nu} - \mathbf{A}\hat{\mathbf{q}}\|_2^2$ serves as a *regularizing contribution*, *prioritizing smoother solutions* over the rapidly varying ones and acting for all intents and purposes as a *low-pass filter*, decreasing the *condition number.* In fact, the inversion of ill-posed, non-regularized problems is known to *amplify the noise* intrinsically present in $\boldsymbol{\nu}$, thus leading to non-physical solutions even when a minimum-norm solution is found.

The issue opens up questions about how to choose the regularization parameter μ_R. Suzuki [7] suggested to select it as $\mu_R^2 = \varepsilon \max(\text{eig}(\mathbf{A}\mathbf{A}^{\text{H}}))$, with ε ranging from 0.1% to 10% to be chosen in a *heuristic manner.* However, this procedure proved not to be rigorous [25] since the choice of μ_R strongly influences the results. Zamponi [18] pointed out the necessity to implement an automated selection process for the parameter and compared three different strategies present in literature suitable to eq. (4.17): Generalized Cross-Validation (GCV), L-Curve method and Quasi-optimality criterion (based on the work [26] by Hansen). Of these, the Quasi-optimality criterion was found to perform better in GIBF's purposes and is thus implemented in the code. It consists in finding a trade-off between perturbation and regularization errors in $\hat{\mathbf{q}}^{(2)}$ by finding

$$\mu_R = \operatorname{argmin} \left\{ \mathbf{G}(\mu) = \mu \left\| \frac{\mathrm{d}\hat{\mathbf{q}}^{(2)}}{\mathrm{d}\mu} \right\| \right\} \tag{4.18}$$

a detailed explanation of the three methods is discussed in [27].

Given the regularization parameter μ_R, the solution to equation (4.17) is provided analytically:

$$\hat{\mathbf{q}}^{(2)} = \mathbf{A}^{\mathrm{H}}(\mathbf{A}\mathbf{A}^{\mathrm{H}} + \mu_R^2 \mathbf{I})^{-1} \boldsymbol{\nu} \tag{4.19}$$

4.7.2 $\mathcal{L}^1$ norm minimization via IRLS algorithm

As previously stated, $\hat{\mathbf{q}}^{(2)}$ represents the starting point for an iterative process aiming to seek the $\mathcal{L}^1$ minimum-norm solution to eq. (4.8), i.e.

$$\hat{\mathbf{q}}^{(1)} = \operatorname{argmin} \left\{ \mu_R^2 \|\hat{\mathbf{q}}\|_1 + \|\boldsymbol{\nu} - \mathbf{A}\hat{\mathbf{q}}\|_1^2 \right\} \tag{4.20}$$

where $\| \cdot \|_1$ stands for the 1-norm (sum of the vector's elements). Here, following Suzuki, the *Iterative Re-weighted least squares* (IRLS) algorithm [28] is implemented. The method consists in computing the α-th iteration as:

$$\hat{\mathbf{q}}_{\alpha+1} = \mathbf{W}_\alpha \mathbf{A}^{\mathrm{H}}(\mathbf{A}\mathbf{W}_\alpha \mathbf{A}^{\mathrm{H}} + \mu_{R,\alpha}^2 \, \mathbf{I})^{-1} \boldsymbol{\nu} \tag{4.21}$$

where $\mathbf{W}_\alpha = \operatorname{diag}(|\hat{q}_{\alpha,1}|, ..., |\hat{q}_{\alpha,n}|)$ is the diagonal matrix whose components are the amplitudes of the elements in $\hat{\mathbf{q}}_\alpha$ (the α-th iterate), provided that $\hat{\mathbf{q}}_0 = \hat{\mathbf{q}}^{(2)}$, i.e. the starting iterate is the $\mathcal{L}^2$ minimum-norm solution of eq. (4.8). The iteration process stops when:

- the cost function in eq. (4.20) starts increasing or
- or the iteration counter reaches a pre-defined limit.

At the end, the solution to eq. (4.20) is obtained as $\hat{\mathbf{q}}^{(1)} \equiv \hat{\mathbf{q}}_\alpha$, where α stands for the last iteration number. In eq. (4.21), the IRLS regularization parameter $\mu_{R,\alpha}$ is to be determined before *every iteration*, thus the methods introduced for the $\mathcal{L}^2$-norm minimization cannot be applied. Therefore, it is imposed that

$$\mu_{R,\alpha}^2 = \varepsilon \max(\operatorname{eig}(\mathbf{A}\mathbf{W}_\alpha \mathbf{A}^{\mathrm{H}})) \tag{4.22}$$

where the regularization parameter $\mu_{R,\alpha}^2$ is intended as a fraction of the greatest eigenvalue of $\mathbf{A}\mathbf{W}_\alpha \mathbf{A}^{\mathrm{H}}$ via a user-imposed value of ε, ranging from 0.1% to 10%.

4.7.3 Iterative dimensionality reduction

To lighten the memory dedicated to code execution and save computational time, as well as to promote sparsity, on every α-th iteration a user-defined fraction β (with $0 < \beta < 1$) of the components of the source-amplitude vector $\hat{\mathbf{q}}_\alpha$ are kept (those with greater amplitude) while the smallest ones are discarded and equaled to zero, so that at the α-th iteration, $\mathbf{A}$ will have dimensions $M \times (\beta^\alpha N)$ and $\hat{\mathbf{q}}_\alpha$ will contain $\beta^\alpha N$ elements instead of the original size of N elements. This process continues until a minimum number of point sources, decided by the user as a fraction of N, is reached. It is crucial to highlight that the number $\beta^\alpha N$ of non-discarded sources must not drop beneath the number of microphones M, as the dimensions would result in the problem in eq. (4.8) being overdetermined, necessitating the application of a solution algorithm appropriate for such a scenario. Finally, the *iterative dimensionality reduction* process is optional and is only motivated by computational needs.

4.7.4 Extension to $\mathcal{L}^p$-norm minimization

The mathematical problems described in eqs. (4.17)(4.20) belong to the class of the *optimization problems*, in which a solution that minimizes/maximizes a certain *cost function* is to be found iteratively in the general case. Precisely, the cost function here involved is of the kind:

$$J_p = \mu_R^2 \|\hat{\mathbf{q}}\|_p^p + \|\boldsymbol{\nu} - \mathbf{A}\hat{\mathbf{q}}\|_p^2 \tag{4.23}$$

where subscript p here denotes the p-norm of a vector and J_p represents the cost function to be minimized when the $\mathcal{L}^p$ minimum-norm solution to a underdetermined problem (such as eq. (4.8)) is sought. In *compressed sensing* problem as GIBF, $\mathcal{L}^p$ minimum-norm solutions $\hat{\mathbf{q}}^{(p)}$ with $0 < p < 1$ (e.g. $p = 0{,}9$) proved to be effective in sparse source recovery, because of a even greater capacity to promote sparsity in the sound maps with respect to $\mathcal{L}^1$-norm solutions. The IRLS method can be generalized to solve any kind of J_p minimization problem, leading to the following expression for the α-th iteration towards $\hat{\mathbf{q}}^{(p)}$:

$$\hat{\mathbf{q}}_{\alpha+1} = \mathbf{W}_\alpha \mathbf{A}^{\mathrm{H}} (\mathbf{A}\mathbf{W}_\alpha \mathbf{A}^{\mathrm{H}} + \mu_{R,\alpha}^2\ \mathbf{I})^{-1} \boldsymbol{\nu} \tag{4.24}$$

where, in analogy with eq. (4.21), $\mathbf{W}_\alpha = \mathrm{diag}(|\hat{q}_{\alpha,1}|^{2-p}, ..., |\hat{q}_{\alpha,n}|^{2-p})$ is the diagonal matrix whose components are the amplitudes of the elements in $\hat{\mathbf{q}}_\alpha$ (the α-th iterate) elevated to $2 - p$. Again, the solution to eq. (4.17) can be exploited as the starting iterate.

4.8 EXTENSION TO 3D GIBF FOR CAA-BASED BEAMFORMING

The development of a 3D beamforming method represents a significant advancement in the field due to its capability to enhance the localization precision of acoustic sources in array processing applications. Traditional two-dimensional beamforming techniques have limitations in accurately determining the position of sound sources, particularly in scenarios where sources exist in three-dimensional space or where the environment introduces complex acoustic phenomena. By extending beamforming into the third dimension, the system gains the capability to capture the depth component of sound sources, thus providing a more comprehensive spatial understanding.

As stated in sec. 4.1, with respect to *conventional beamforming*, that lays upon the hypothesis that the resolved source is solely present in the interrogated region, GIBF considers the whole set of grid-defined acoustic sources at one time, so that its solution distributes the detected acoustic energy among the user-discretized point sources close to the physical source, and the source amplitude's estimation will result from their summation (refer to eq. (4.9)).

This important property enables the GIBF algorithm to be employed for a 3D point grid with no further efforts. Since, in the present work, the propagation is modeled source-to-microphone without any other assumptions on their location, one can easily discretize a spatial region through a three-dimensional point grid implement a three-dimensional and solve eq. (4.4) for the source-strength vector $\hat{\mathbf{q}}$, provided that the transfer matrix $\mathbf{A}$ is arranged to model the wave paths of each source-microphone combination.

However, it is important to consider that the algorithm's ability to capture the depth of the source position is closely related to the *characteristics of the array*, *which must at least also extend in the direction of depth*, in order to obtain physically relevant solutions. This complicates matters in wind tunnel experimentation, where it is not always possible, for reasons of cost or lack of space, to have multi-dimensional arrays, reason why 3D beamforming is not yet common in experiments involving real-world measurements. Instead, multi-dimensional arrays are easily employed in CAA-based measurements since no line is drawn to the researcher, so that the present approach seems to be more addressed to those, despite being theoretically suitable to either experimental and numerical investigations.

Chapter5

IMPLEMENTATION

In this chapter, the implementation of GIBF *tool* will be examined and its features will be showcased.

5.1 A MATLAB UI-BASED APP

The development of a GIBF *tool* was driven by the necessity of enabling fast and reliable beamforming analysis in aeroacoustic applications and making the results accessible to the researcher quickly. The implementation had to include a graphical user interface to simplify the preparation of the calculation and make it guided, so that the user only has to provide the necessary input for the analysis.

To accomplish these tasks, the author opted for a MATLAB implementation using the *App Designer Toolbox* to generate the graphical interface. The code is fully vectorized and parallelized using the *Parallel Computing Toolbox*, thus enabling a better CPU usage. It is organized in tabs to best guide the user through the beamforming procedures.

5.2 TAB: GRID SETUP

In this tab, showed in fig. 5.1, the user has the possibility of determining the characteristics of the source point grid to be used. This is done in terms of the *spatial resolution* of the point sources, the *extent* of the grid and the *position of its centre*. By specifying the third dimension, a three-dimensional point grid is generated and a 3D beamforming computation is automatically queued.

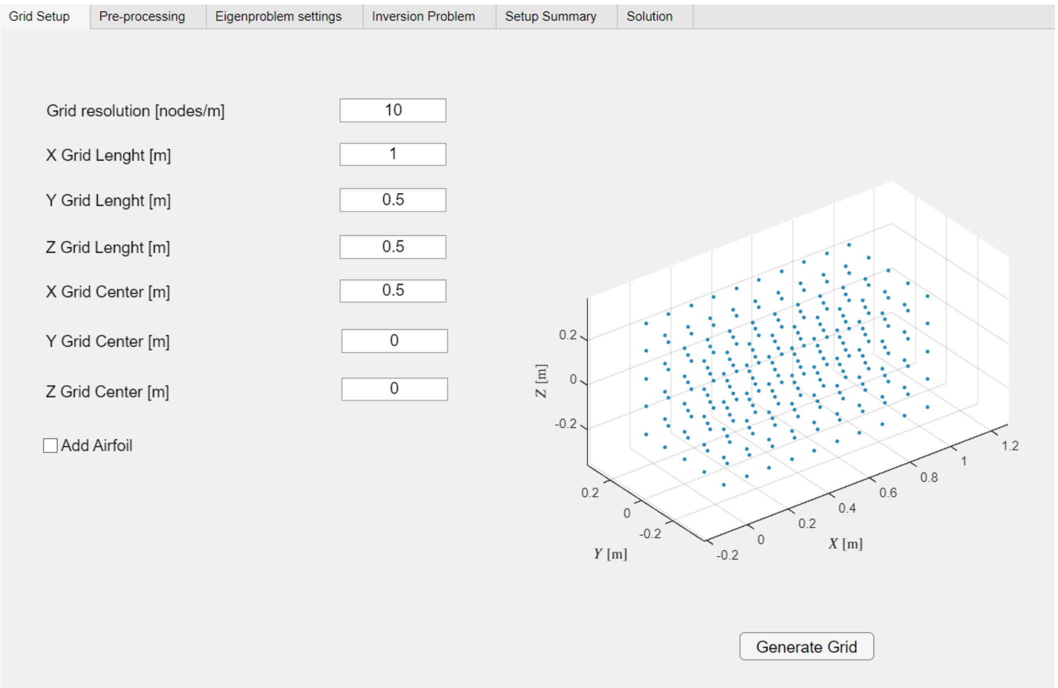

Grid resolution [nodes/m] 10
X Grid Lenght [m] 1
Y Grid Lenght [m] 0.5
Z Grid Lenght [m] 0.5
X Grid Center [m] 0.5
Y Grid Center [m] 0
Z Grid Center [m] 0
☐ Add Airfoil

Figure 5.1: View of the grid generation tab in GIBF *tool*.

Parameter	Value
Default window size	4096 samples
Windowing method	*Hamming*
Window overlap	50%
Sampling frequency	*User-defined*

Table 5.1: Parameters for the CSM computation using `pwelch` routine.

5.3 TAB: PRE-PROCESSING

In this tab, with reference to fig. 5.2 the user is asked to provide the main inputs for the computation. Firstly, the microphone recordings can be submitted uploading both the pre-computed CSM or the time-domain recording of the array's microphone. In the second case, the *tool* is able to calculate the CSM using the Welch's method via the `pwelch` MATLAB® routine, adopting the standard parameters given in table 5.1, where the user only has to provide the *sampling frequency* of the microphone recordings and the *window size* to operate the FFT. Then, the user has to provide the array's coordinates in a text file (with the possibility to adopt a multiple array configuration). The correction for convection velocity can be accounted for by supplying the free-stream velocity in terms of magnitude and direction, while the shear layer correction can be added with the Mach correction factor in eq. (4.16). Finally, the frequency to analyse are asked, with the possibility to opt for a narrow frequency or a one-third frequency band analysis.

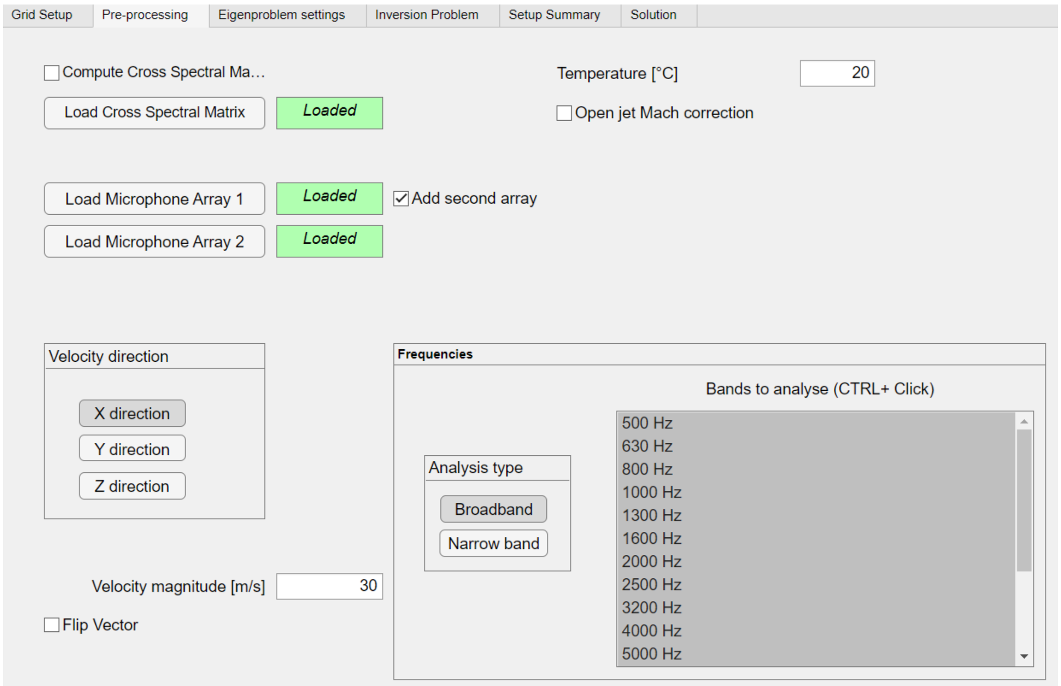

☐ Compute Cross Spectral Ma...

Temperature [°C] 20

☐ Open jet Mach correction

☑ Add second array

Velocity magnitude [m/s] 30

☐ Flip Vector

500 Hz
630 Hz
800 Hz
1000 Hz
1300 Hz
1600 Hz
2000 Hz
2500 Hz
3200 Hz
4000 Hz
5000 Hz

Figure 5.2: View of the pre-processing tab. Here the user is asked to provide the main inputs for the computation.

5.4 TAB: Setup Summary

This tab (fig. 5.3) is intended to show an overview of the settings used for the analysis the user intends to run. On the left side, a brief summary of the grid's and the array's characteristics is provided. Additionally, the flow's free-field conditions for accounting for *speed of sound*, *convection effects* and, eventually, the presence of a *shear layer* (in wind tunnel applications) are specified. On the right side, a graphical overview of the computational domain is shown to allow the user to check the domain's geometrical features.

5.5 TAB: Inversion Problem

Here (ref. fig. 5.4) the researcher can decide the IRLS parameters for the queued GIBF analysis. Firstly, the user has to choose between a monopole or a dipole beamforming analysis. Then, the regularization parameter ε, the reduction factor β and the minimum number of the non-discarded sources in percentage of the grid point number are tuned. Finally the p-norm minimization is defined.

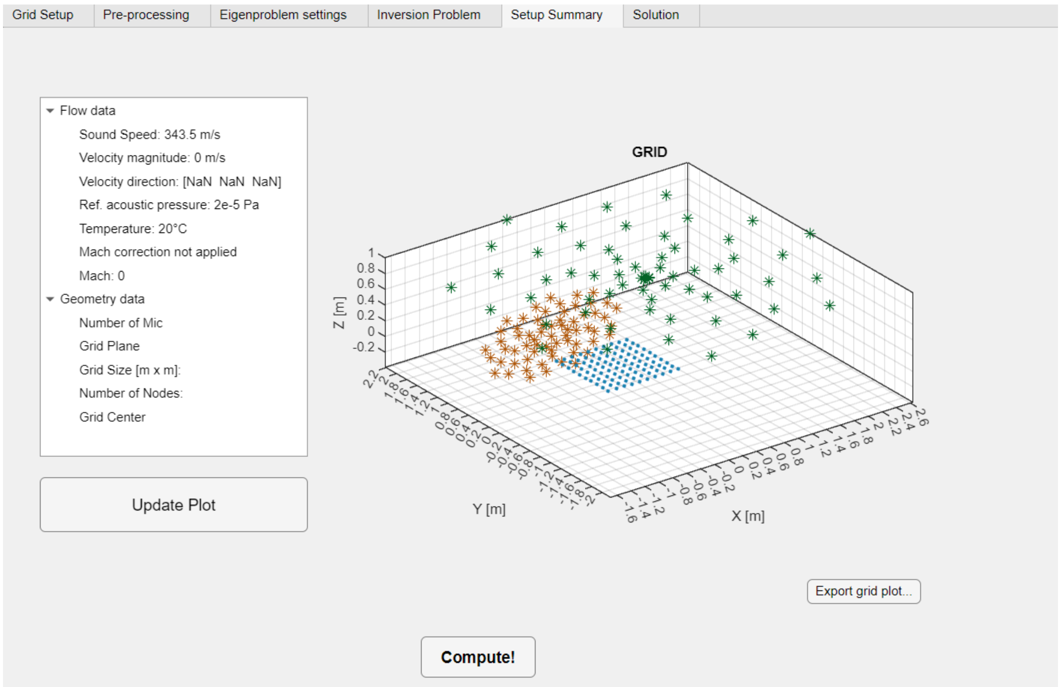

- Flow data
  - Sound Speed: 343.5 m/s
  - Velocity magnitude: 0 m/s
  - Velocity direction: [NaN NaN NaN]
  - Ref. acoustic pressure: 2e-5 Pa
  - Temperature: 20°C
  - Mach correction not applied
  - Mach: 0
- Geometry data
  - Number of Mic
  - Grid Plane
  - Grid Size [m x m]:
  - Number of Nodes:
  - Grid Center

Figure 5.3: View of the setup summary tab, where the geometry of the domain is summarized. Sources are indicated with blue dots while asterisks indicate the two arrays' microphones, for which different colors are employed.

Algorithm Choice

● Tikhonov
○ Bayesian

Source type

● Monopole
○ Dipole

☐ Multi-thread mode

Number of Workers 1

IRLS Algorithm Off ● On

L^p-norm minimization 1.0

Figure 5.4: View of the inversion problem tab, where the user can indicate the IRLS parameters.

Chapter6

SIMULATIONS AND BENCHMARKS

To assess the characteristics of the algorithm and the performance of its implementation, namely the GIBF *tool*, a series of benchmarks is here reported. As an instructive test case, the beamforming of a synthetic monopole is run in section 6.1 using a planar array. Subsequently, in sec. 6.2 the new capabilities afforded by extending beamforming to three-dimensional grid domains and multipole detection are explored (ref. sec. 4.8,4.4). Finally, in section 6.3 the GIBF tool is applied to the real-life case of *cylinder noise* using wind tunnel measurements, where the corrections studied in sec. 4.5 and 4.6 will be essential.

6.1 BEAMFORMING OF A SYNTHETIC MONOPOLE

The beamforming of a simple synthetic monopole emitting two *tonal frequencies* is executed. After adjusting the settings, the code is run and the subsequent sound maps in output are evaluated. Then, the source quantification is compared with the microphone-recorded SPL at a reference distance. This benchmark also aims to explore the results' variations due to different values of ε, whose selection is not automatic but left to the user. Additionally, GIBF's response to noise is investigated.

6.1.1 Benchmark description

The acoustic pressure field of a synthetic monopole located in $(0, 0, 0)$m is generated numerically, exploiting the following expression for a *harmonic monopolar field* is:

$$p'(r,t) = \frac{Q}{4\pi r}\cos\left(2\pi f t - kr + \phi\right) \tag{6.1}$$

where Q [Pa m] is the source strength of the monopole, and $k = \frac{\omega}{c_0} = \frac{2\pi f}{c_0}$ is the wave number (the speed of sound c_0 is assumed to be 340m s^{-1}).

Here, the monopole is thought to emit the sum of two separate-frequency harmonic waves with zero phase delay:

$$p'(r,t) = \frac{Q_1}{4\pi r}\cos\left(2\pi f_1 t - k_1 r\right) + \frac{Q_2}{4\pi r}\cos\left(2\pi f_2 t - k_2 r\right) \tag{6.2}$$

The parameters are reported in table 6.1. The signal $p'(r,t)$ in eq. (6.2) is recorded by a 64-microphones planar array, positioned at a distance of 1m, with a sampling frequency $f_S = 7000$Hz to be compliant with the *Nyquist–Shannon sampling theorem*, and in a total of 10^4 samples collected. To ensure the whole acoustic energy is enclosed in the computational domain, a $1\text{m} \times 1\text{m}$ grid of resolution 30 sources/m is adopted, and centered on the monopole sought, i.e., in the axes' origin. The situation is represented in fig. 6.1.

6.1.2 GIBF settings

Firstly, the CSM matrix must be computed via *Welch's method*. A number of 4096 samples per microphone is considered, and hamming windowing is applied, with a 50% overlap between them. The whole process is executed under the GIBF *tool*'s body. As it is obvious, GIBF *tool* is set to look for monopolar sources in the 800Hz − 3200Hz frequency range, so that the **A** matrix modeling the source-microphone sound propagation is filled with the elements shown in eq. (4.2). Since the synthetic monopole is believed to be the only source in the domain, *the sole first eigenmode is considered*. In particular, a $\mathcal{L}^1$ minimum-norm solution is sought, therefore IRLS algorithm resolving shown in eq. (4.20) is applied, with a maximum number of iterations of 50 to keep computation times short. After each iteration, the number of point sources is reduced of a factor $(1 - \beta) = 5\%$ (see sec. 4.7.3), until a minimum number of $N/2$ sources is reached, where N is the number of sources given by the point grid. Regarding the discarded sources, a null amplitude is assigned to them. The $\mathcal{L}^2$ regularization factor μ_R is computed through the *quasi-optimality criterion* (4.18), while the $\mathcal{L}^1$ regularization factor $\mu_{R,\alpha} = \varepsilon \max(\text{eig}(\mathbf{A}\mathbf{W}_\alpha\mathbf{A}^\text{H}))$, with ε chosen *heuristically*, as stated in sec. 4.7. After presenting the results, the role of ε in source quantification will be discussed in sec. 6.1.4.

6.1.3 Results

Fig. 6.2 shows the outcomes of the GIBF *tool* in the monopole case. Regardless of the choice of ε, the source localization process always converges to finding a monopole in the axes' origin. Hence, the regularization parameter seems not to be crucial in recovering the source's position. Rather, it is source-amplitude reconstruction that is most influenced by ε and thus requires a special care (this aspect will be covered in sec. 6.1.4). To find out the most appropriate value of ε, the overall source amplitude $\hat{Q}$ can is recovered *by summing the resolved point sources*, as demonstrated in eq. (4.9). Then it is propagated towards the array

Parameter	Symbol	Value
Source Amplitude for f_1	Q_1	$4\pi \cdot 2\mathrm{Pa\,m}$
Source Amplitude for f_2	Q_2	$4\pi \cdot 5\mathrm{Pa\,m}$
SPL at 1m for f_1	SPL_1	92dB
SPL at 1m for f_2	SPL_2	105dB
Emitted frequency 1	f_1	1000Hz
Emitted frequency 1	f_2	3000Hz
Sampling frequency	f_S	7000Hz
Number of samples	n_S	10^4
Sampling time	t_S	1,42s
Array distance	r_A	1m
Array diameter	D_A	4,5m
Number of microphones	M	64
Number of sources	N	900

Table 6.1: Selected parameters for the synthetic monopole simulation.

Grid description	
Dimensions	$1\mathrm{m} \times 1\mathrm{m}$
Plane	$x - y$
Origin	$(0, 0, 0)\mathrm{m}$
Resolution	30 sources/m
Number of sources	900

Table 6.2: Characteristics of the computational grid adopted.

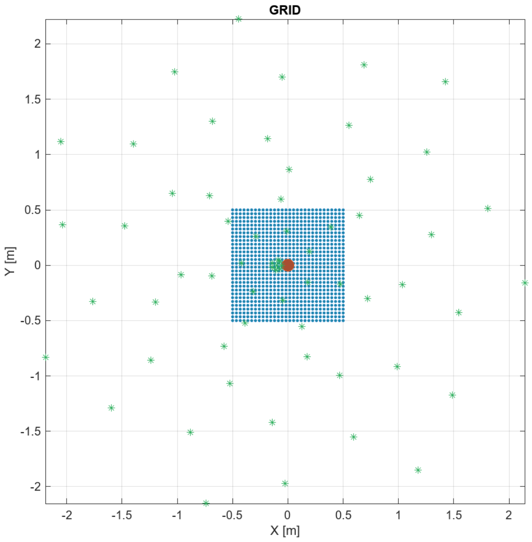

Figure 6.1: Computational domain adopted for the simulation, generated within the GIBF *tool*. The orange circle stands for the source's position, while the green markers represent the array's 64 microphones. Each of the blue dots is a point source the solver takes into account.

(via the well-known monopolar source-microphone transfer function in eq. (4.2)) and the resulting SPL trend is compared with the one coming from the central microphone's signal, looking for the ε value for which the two of them overlap. The procedure, whose result is reported in fig. 6.3, led to a optimal value of $\varepsilon = 10\%$. It can be seen that, even using the optimal value of ε, GIBF *slightly overestimates the high-frequency peak*, a phenomenon that is frequently encountered. Thus it is not possible to select a value of ε capable to match the two peaks simultaneously.

6.1.4 Response to regularization factor variations

To obtain insight about the most appropriate regularization factor in IRLS algorithm, a parametric study on the regularization factor is carried out through the tuning of ε. Several values of the parameter in the range $0{,}1\% < \varepsilon < 10\%$, as suggested by Suzuki, are considered to gain comprehension about its role in source quantification, after its minor effect on localization has been proved in sec. 6.1.3. Focusing on the 1000Hz peak, results in fig. 6.4 show that, even though the obtained SPL trends predicted by GIBF at a distance of 1m approach the exact value of 92dB given by the array's central microphone, the proposed method of selection of ε is not satisfactory and there is a need to introduce a *more robust algorithm* of regularization.

6.1.5 Response to noisy measurements

In this section, it will be shown the behaviour of the code with respect to *Gaussian random background noise* in measurements. In general, the linear system in eq. (4.4), when characterized by measurement noise $\boldsymbol{\gamma}$, can be seen as:

$$\mathbf{p} = \mathbf{A} \cdot \mathbf{q} + \boldsymbol{\gamma} \tag{6.3}$$

Since measurement noise is a natural process, i.e. unbiased and normally distributed, $\boldsymbol{\gamma}$ can be thought as

$$\boldsymbol{\gamma} \sim \mathcal{N}(0, \sigma_\gamma^2) \tag{6.4}$$

where $\mathcal{N}(0, \sigma_\gamma^2)$ represents the normal distribution of zero mean and variance σ_γ^2. In this context, σ_γ^2 is determined through a user-defined *signal-to-noise* (SNR) ratio:

$$\mathrm{SNR} = \frac{\sigma_p^2}{\sigma_\gamma^2} \tag{6.5}$$

where σ_p^2 has been determined as the monopole-generated signal's variance at the array's distance r_A:

$$\sigma_p^2 = \frac{1}{2}\left(\frac{Q_1}{4\pi r_A}\right)^2 \tag{6.6}$$

Practically, to generate noisy signals, at each microphone numerically-computed n-th pressure signal p_n' is summed a random noise contribution γ_n, by applying the formula:

$$p_n = \frac{Q}{4\pi r_n} \cos\left(2\pi f t - k r_n\right) + \gamma_n \tag{6.7}$$

where

$$\gamma_n \sim \mathcal{N}\left(0, \frac{\sigma_p^2}{\mathrm{SNR}}\right) = \sqrt{\frac{1}{\mathrm{SNR}}} \frac{Q}{4\pi r_n} \cdot \mathcal{N}(0,1) \tag{6.8}$$

In contrast to the de-noised case, here the focus is solely on the Q_1 monopole, which radiates at a frequency of 1000Hz. The examination involves the manipulation of the SNR parameter while maintaining $\varepsilon = 10\%$ constant, identically to the value that yielded the most optimal outcome in the scenario without background noise. Fig. 6.5 displays the results obtained: GIBF *tool*'s algorithm has no problem in localization of the monopolar source in the axes' origin, even when noise level is the highest, i.e. $\mathrm{SNR} = 1$.

Again, the reconstructed source amplitude, given by the sum of the point sources on the grid, is propagated towards the array and the resulting SPL is compared to the central microphone's SPL distribution over frequency. With reference to fig. 6.6, the GIBF *tool* seems to be not particularly disturbed in the basic scenario of an isolated monopole, when confronted with random background noise during measurements. The presence of the monopole is still illustrated by the peak observed at 1000Hz. Furthermore, it is apparent that upholding a regularization parameter identical to that of the de-noised scenario results in a solution deemed more than satisfactory even amidst noisy conditions, with a peak that marginally diminishes in the presence of disturbances of a magnitude comparable to that of the target source, for $\mathrm{SNR} = 1$. Although noise is also present in GIBF's reconstruction, it is visibly lower with respect to recorded signal's one because of its incompatibilities with meaningful, actual sources.

GIBF Settings	
Norm minimization	$\mathcal{L}^1$
Reduction factor β	95%
Min. number of sources	$N/2$
Number of eigenmodes	1
μ_R selection	quasi-optimality
ε selection	heuristic

Table 6.3: Description of the GIBF settings applied.

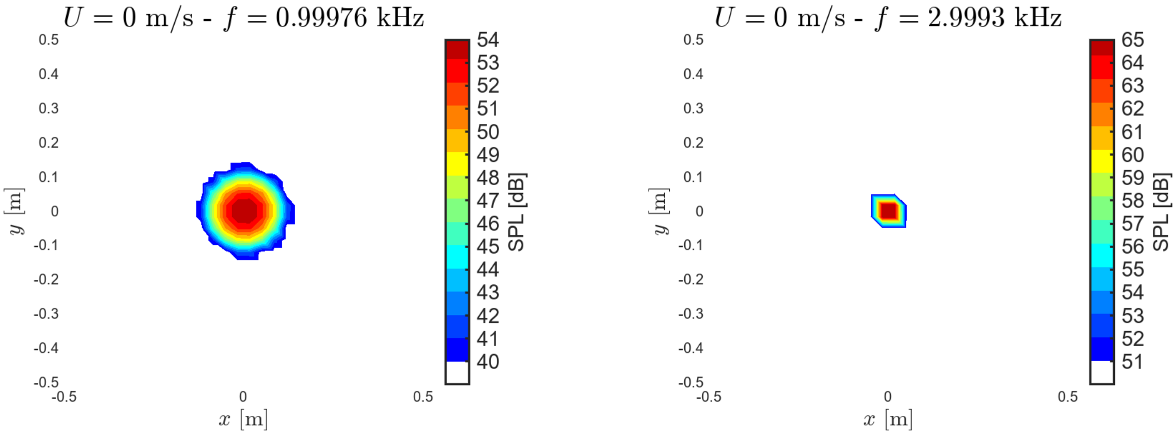

(a) $f = f_1 = 1000$Hz

(b) $f = f_2 = 3000$Hz

Figure 6.2: Sound maps generated by GIBF *tool* for the synthetic monopole case, obtained for $\varepsilon = 10\%$. Sources are displayed within a dynamic range of 15dB from the greatest point source. SPL is computed by propagating the reconstructed source towards the array's central microphone.

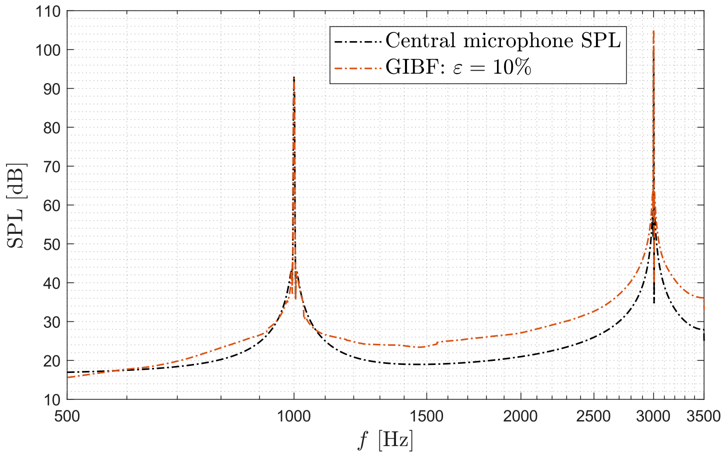

Figure 6.3: Comparison between the central microphone's SPL distribution over f and the GIBF solution propagated towards the array, for $\varepsilon = 10\%$. The graph shows a perfect overlap of the two trends.

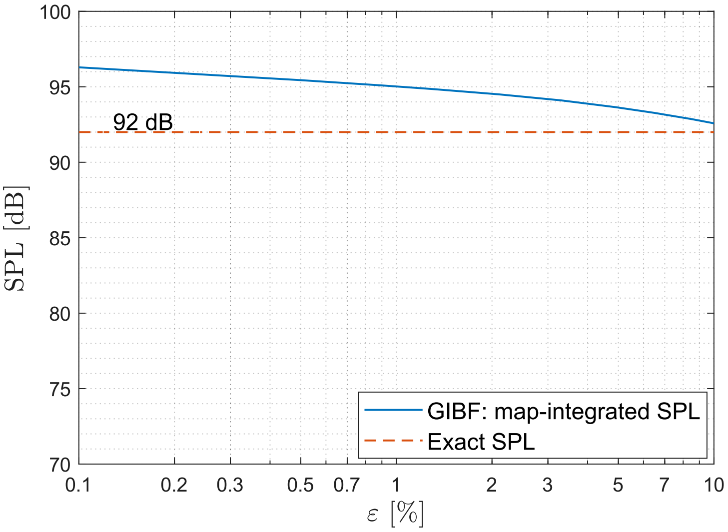

Figure 6.4: Map-integrated peak SPL at $f = 1000$Hz as a function of regularization parameter ε. Results show ε having the effect of lowering the retrieved acoustic energy in the GIBF solution. However, no ε value in the range identified by Suzuki (sec. 4.7) is capable of returning an adequate SPL estimate.

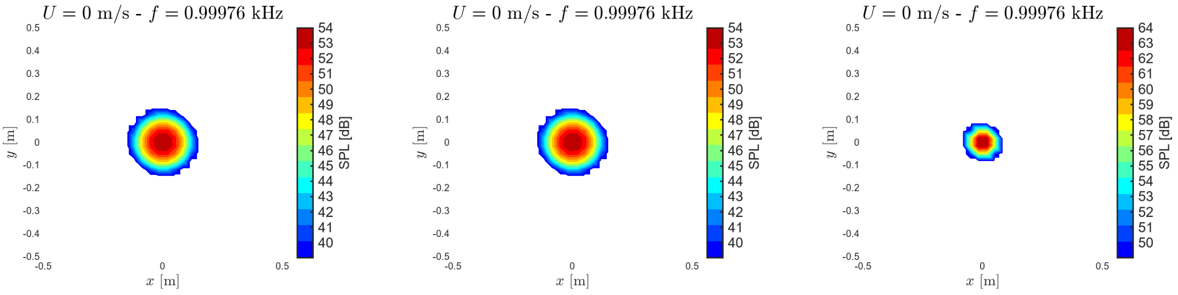

(a) SNR = 3

(b) SNR = 2

(c) SNR = 1

Figure 6.5: Sound maps computed for $f = f_1 = 1000$Hz and $\varepsilon = 10\%$ at different SNRs, sorted from the simplest to the hardest case, and displayed in a dynamic range of 15dB. Even in presence of a strong noise variance, $\sigma_\gamma^2 = \sigma_p^2$ for the SNR = 1 case, the GIBF's source reconstruction appears not to be significantly affected by noise.

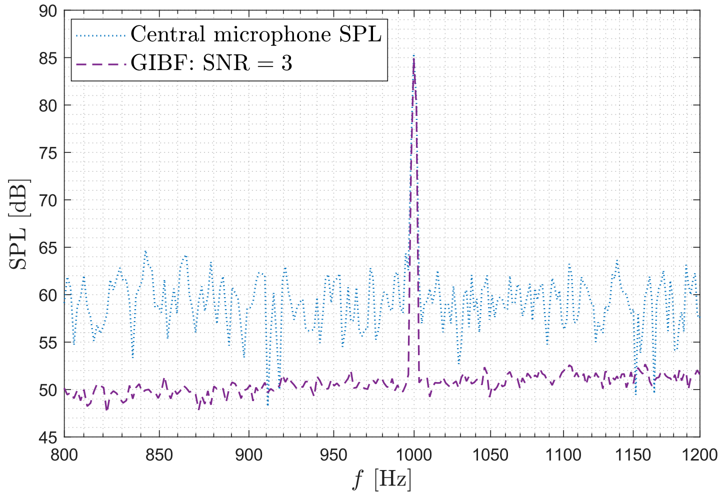

(a) SNR = 3

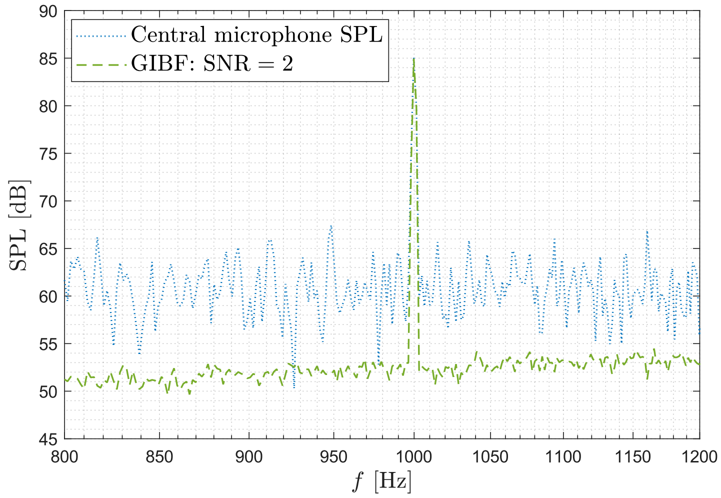

(b) SNR = 2

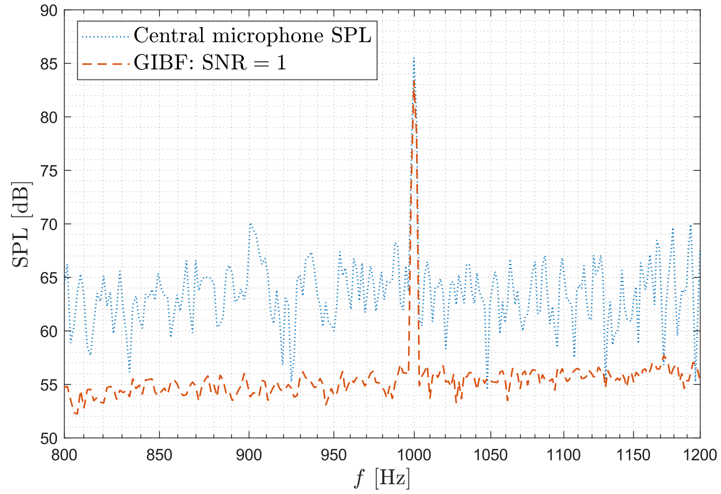

(c) SNR = 1

Figure 6.6: Comparison between SPL computed from map-integrated point sources ($\varepsilon = 10\%$) and that from the central microphone's recording, for different levels of SNR.

6.2 BEAMFORMING OF TWO FREELY ORIENTED DIPOLES

The aim of the benchmark is to showcase the capability of GIBF in ascertaining the spatial positioning of a *distribution of freely oriented dipoles*, a scenario which could make things difficult for alternative beamforming techniques. Moreover, this task is carried out not solely on a two-dimensional computational point grid, but also employing a *three-dimensional grid*.

6.2.1 Benchmark description

Two synthetic dipoles, namely a x-oriented dipole and a y-oriented dipole, positioned in $(0.3, 0, 0)$m and $(-0.3, 0, 0)$m respectively, emit sound waves at a frequency $f = 1000$Hz. Their signals at each microphone are numerically generated using the *far-field approximation of a dipole-type acoustic field*:

$$p'(\mathbf{r}, t) = \frac{Q_{\text{dip}}}{4\pi\|\mathbf{r}\|}\left[\boldsymbol{\zeta} \cdot \frac{\mathbf{r}}{\|\mathbf{r}\|}\right]\cos\left(\omega t - k\|\mathbf{r}\|\right) \tag{6.9}$$

where $\mathbf{r} = \mathbf{x} - \mathbf{x}_0$ is the source-receiver distance vector (dipole being located in $\mathbf{x}_0$), $\boldsymbol{\zeta}$ is a unitary vector representing the *dipole axis' orientation*, and Q_{dip} is the dipole strength to be recovered. At the microphones, the linear superposition of the two dipoles' fields is observed. The sources' directivities suggest the adoption of a *multi-dimensional microphone array*, that GIBF *tool* can easily handle. In fact, dealing with a computational environment enables the use of the most appropriate array geometry without the typical difficulties of experimentation. Hence, the emitted sound waves are simultaneously recorded by an array of 80 microphones randomly distributed on a sphere of radius $r_A = 5$m (illustrated in fig. 6.8). In analogy with the monopole case (sec. 6.1), the signal is captured with a sampling frequency of $f_S = 7000$Hz for a total of 10^4 samples. Two point grids are considered: a simple planar $1\text{m} \times 1\text{m}$ $x - y$ grid and a three-dimensional $1\text{m} \times 1\text{m} \times 1\text{m}$ grid, each of them being centered in $(0, 0, 0)$m and having resolution 30sources/m. The two grids adopted are represented in fig. 6.7, while the choices adopted for the simulation parameters are shown in the tab. 6.4.

6.2.2 GIBF settings

The *pre-processing phase* to obtain the CSM is the same as sec. 6.1.2. The configurations of the linear problem inversion algorithm remain consistent with those utilized for the monopole and are delineated in sec. 6.1.2 providing a comprehensive explanation. Table 6.3 is also available for readers seeking an overview of these configurations. In this instance, the *multipole detection algorithm* (refer to se. 4.4) is enabled, enabling the identification of the location of freely distributed dipoles with varying directivity in three-dimensional space, attributing the existence of *three overlapping dipoles sources* (oriented in the three axes' directions) to

Parameter	Symbol	Value
Dipolar Source Amplitude	Q_{dip}	2Pa m
SPL at 5m for $f = 1000$Hz	SPL	61dB
x-dipole's position	$\mathbf{x}_{0,x}$	$(0.3, 0, 0)$m
y-dipole's position	$\mathbf{x}_{0,y}$	$(-0.3, 0, 0)$m
Emitted frequency	f	1000Hz
Sampling frequency	f_{S}	7000Hz
Number of samples	n_{S}	10^4
Sampling time	t_{S}	1,42s
Array distance	r_A	5m
Number of microphones	M	80

Table 6.4: Selected parameters for the synthetic monopole simulation.

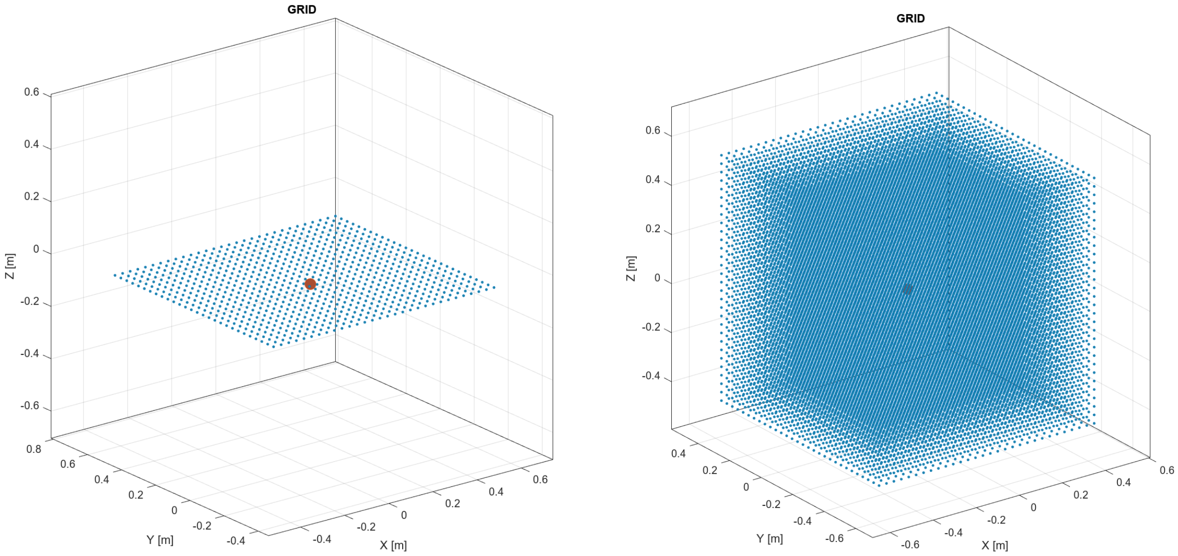

(a) 2D-GRID: 1m × 1m $x - y$ grid centered in $(0, 0, 0)$m with resolution 30sources/m, 3×900 point sources.

(b) 3D-GRID: 1m × 1m × 1m grid centered in $(0, 0, 0)$m with resolution 30sources/m, 3×27000 point sources.

Figure 6.7: Representation of the two grids adopted, where blue dots represent the point sources. In the multipole detection mode, 3 orthogonal dipoles are overlapped on each grid point.

each grid point. The examination is executed within the frequency range of 800Hz − 1200Hz, aligning with the emission spectrum of the sources. Once more, solely the *first eigenmode* is taken into account, as it retrieves the acoustic energy of the two dipoles and is enough to pinpoint their locations.

6.2.3 Results employing a 2D grid

As happened for the monopole case, also in multipole detection for the dipole source recovery the localization resulted not to be influenced by the choice of regularization parameter ε. As showed in fig. 6.9, the two dipolar sources are found where they were supposed to be located, in $(0.3, 0, 0)$m for the x-oriented dipole and in $(-0.3, 0, 0)$m for the y-oriented dipole.

Rather it is the source strength quantification that requires ε to be selected carefully since, as observed in sec. 6.1.3, its value determines the SPL peak value, obtained by summing the point sources on the map as in (4.9). Results are reported in fig. 6.10. Similarly to what happened in the monopole case, the findings illustrate the manner in which, in the context of utilizing a two-dimensional grid, no ε value in the range $0.1\% < \varepsilon < 10\%$ suggested by Suzuki demonstrates the ability to completely recover the acoustic energy resulting from the presence of the two distinct dipoles taken separately, but this time the source strength is always *underestimated*. These dipoles exhibit a SPL equivalent to approximately 61dB at the array's distance, a value known due to the source amplitude assigned for the simulation. Consequently, the smallest ε value, $\varepsilon = 0.1\%$, capable of allocating the maximum SPL and achieving a difference of 3Hz from the exact estimation, is selected.

6.2.4 Results employing a 3D grid

When using the three-dimensional grid in 6.7.b, the GIBF *tool* is capable of reconstructing the source's position in a spatial domain. Maintaining the GIBF's settings unchanged from the two-dimensional grid case (tab. 6.3), even employing a three-dimensional grid the dipoles' localization is impeccable, since the two dipoles are showed in their actual position (refer to 6.11). The exploitation of a 3D results to be beneficial also for source-amplitude estimation. In fact, while the adoption of $\varepsilon = 0{,}1\%$ was insufficient to return the whole dipole's acoustic energy in the two-dimensional point grid case (sec. 6.2.3), using the three-dimensional point grid it retrieves a flawless reconstruction of the source amplitude, the SPL at the array's distance settling around 61dB (with reference to fig. 6.12, where the SPL distribution over frequency is reported).

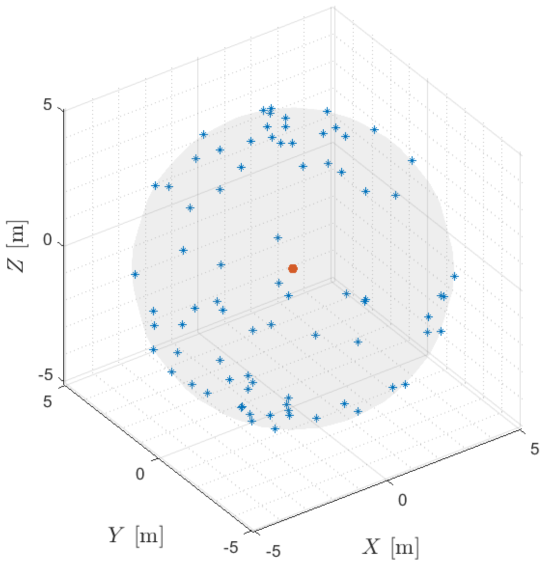

Figure 6.8: Visualization of the spherical array used for the two dipoles benchmark. The array is centered on the axes' origin (represented by the red dot) and its radius $r_A = 5$m. The 80 microphones are randomly distributed on the virtual sphere, allowing complete comprehension of the source directivity.

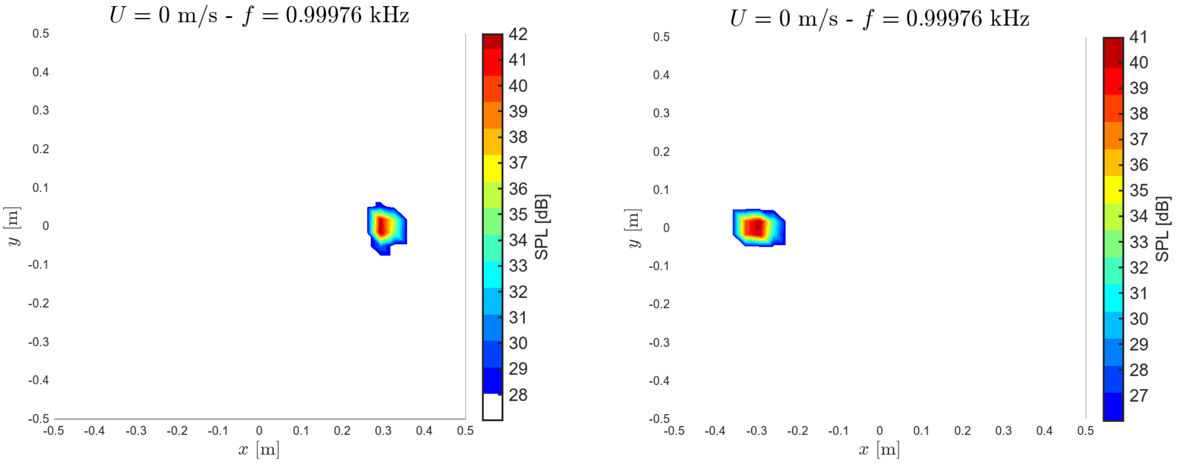

(a) x-oriented dipole

(b) y-oriented dipole

Figure 6.9: Sound maps generated by GIBF *tool* for the two synthetic dipoles case using a two-dimensinal point grid, obtained for $\varepsilon = 0.1\%$ in $f = 1000$Hz. Sources are displayed within a dynamic range of 15dB from the greatest point source. SPL is computed by propagating the reconstructed source towards the array microphones in the dipole's axis direction, which is the direction of maximum amplitude, at a distance of 5m. The maps show a fine reconstruction of both the x-oriented and the y-oriented dipole.

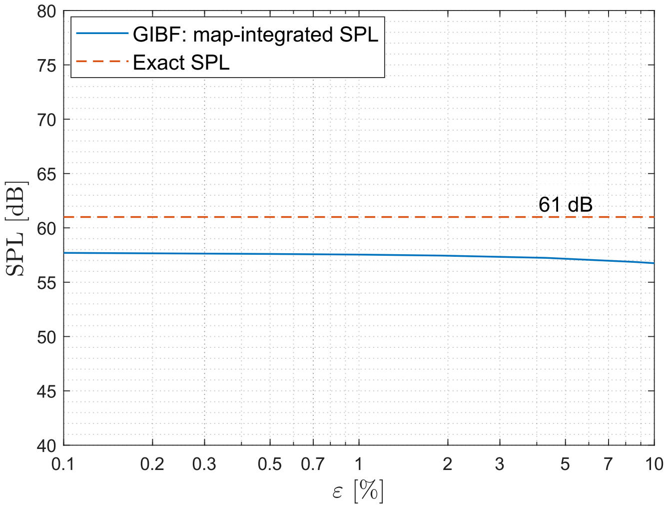

Figure 6.10: Map-integrated peak SPL at $f = 1000$Hz as a function of regularization parameter ε for the 2D grid solution. For the dipole case, similarly to the monopole case, ε has the effect of lowering the retrieved acoustic energy in the GIBF solution. Again, no ε value in the range identified by Suzuki (sec. 4.7) is capable of returning an adequate SPL estimate.

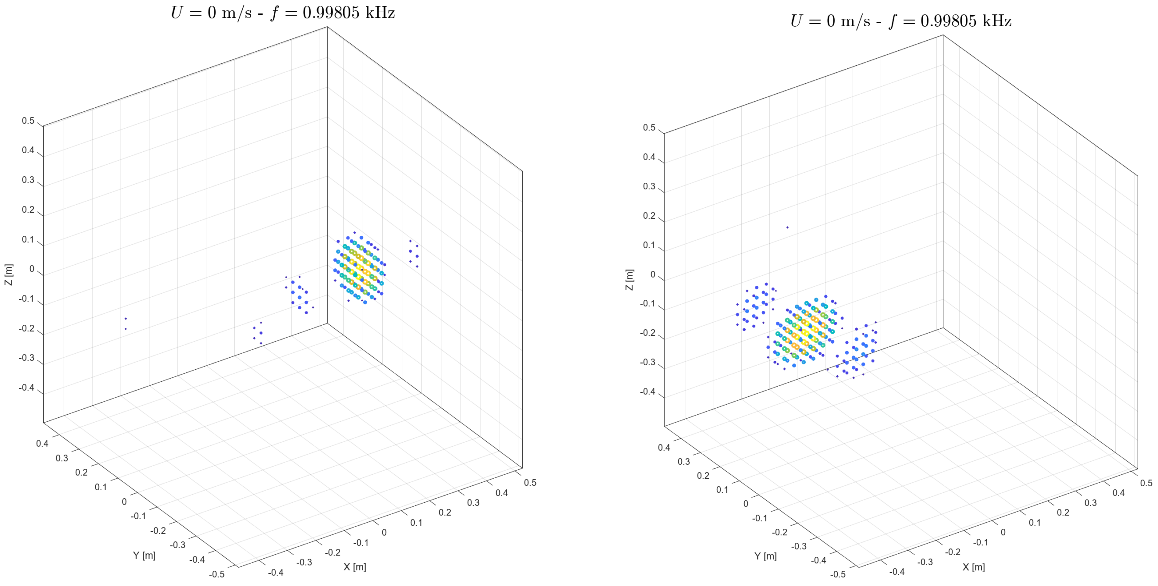

(a) x-oriented dipole

(b) y-oriented dipole

Figure 6.11: Sound maps generated by GIBF *tool* for the two synthetic dipoles case using a three-dimensional point grid, obtained for $\varepsilon = 0.1\%$ in $f = 1000$Hz. SPL is computed by propagating the reconstructed source towards the array microphones in the dipole's axis direction, which is the direction of maximum amplitude, at a distance of 5m. The maps show a fine reconstruction of both the x-oriented and the y-oriented dipole.

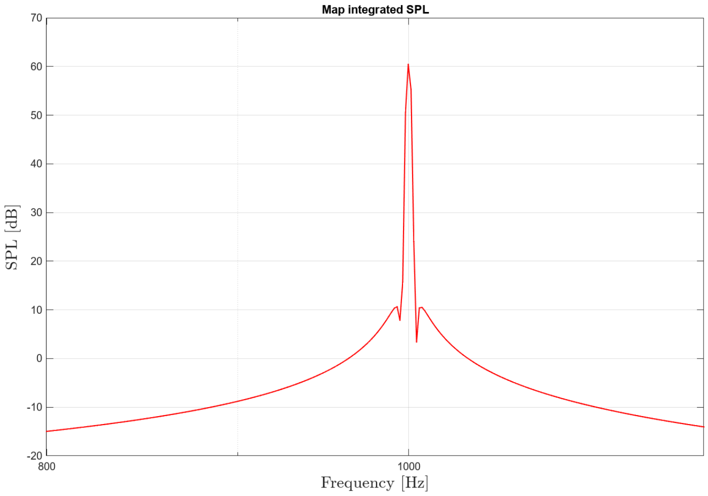

Figure 6.12: GIBF's prediction of the SPL distribution over frequency based on the computed source-strength, using a three-dimensional grid (the trend is identical between the x and the y-oriented dipole). One can notice that in this case the peak SPL approaches the SPL $=$ 61dB (calculated with $p_{\mathrm{REF}} = 20\mu\mathrm{Pa}$) given by the sources imposed for the benchmark.

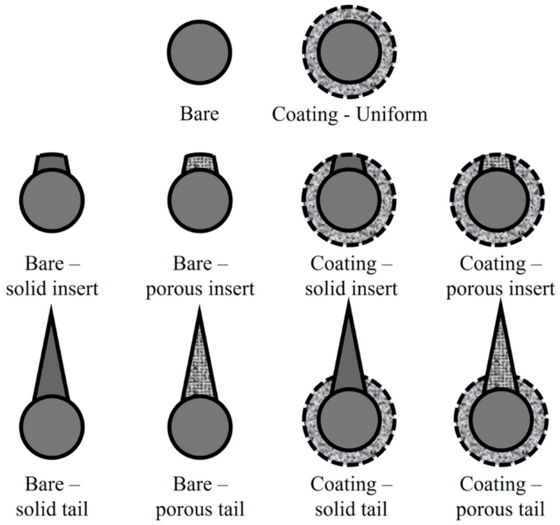

Figure 6.13: Overview of the tested configurations based on the bare and coated cylinders. **Credits**: *Zamponi et al.*

6.3 Beamforming of a coated cylinder's noise

The investigation of cylinder noise is a critical endeavor in the field of fluid dynamics and acoustics. It encompasses the study of sound generated by the interaction of fluid flow with cylindrical structures, which is paramount in various engineering applications, from industrial machinery to aerospace design. Understanding the sound production mechanisms behind the cylinder noise can lead to significant advancements in noise reduction strategies, enhancing the acoustic comfort and reducing the environmental impact of noise pollution.

The noise caused by a cylinder in cross-flow results from the superposition of a broadband component, associated with the turbulent shear layer enveloping the cylinder, and a *tonal component*, referred to as *Aeolian tone* and due to the well-known *vortex shedding*, consisting in the periodic detachment of turbulent eddies at opposite sides of the cylinder. The latter, which represents the major contribution, is also more controllable and thus several studies have been conducted in this sense. In particular, *porous coatings* have been studied extensively due to the findings about their decisive role in decreasing the Aeolian tone peak in emitted sound. It has been proved that this phenomenon is related to the partial *suppression of the unsteady motion* [29], and is explainable in terms of slip velocity and kinetic energy [30].

Zamponi et al. [8] associated this benefit to the porous coatings' ability of shifting downstream the onset location of the vortex street unsteady motion, *point at which the presence of a quadropolar source* can be identified. Hence, the cylinder noise can be explained as the effect of a quadrupolar source in the wake scattering on the cylinder surface resulting in a *dipolar directivity* and to all intents and purposes *improving emission efficiency and increasing perceived noise.* In fact, they demonstrated how this effect can be achieved not only through the use of porous coatings, but also through the insertion of special tails in the back of the cylinder, achieving comparable benefits in terms of noise reduction. Here, a beamforming analysis based on the data collected by Zamponi as part of their research will be carried out to demonstrate the source shifting effect caused by several configurations, as showed in fig. 6.13.

6.3.1 Benchmark description

Measurements were carried in the A-tunnel facility in TU Delft, which is a vertical open-jet wind tunnel placed in a anechoic chamber. The cylinder ($d = 0{,}02$m) is placed inside the chamber and supported by two side plates. With reference to fig. 6.14, reporting the scheme of the experiment's arrangement and the reference system adopted, the x-axis is aligned with the streamwise direction, the z-axis is aligned with the span of the cylinder, and the y-axis is oriented in order to form a right-handed coordinate system. The origin is placed at the midspan of the trailing edge of the cylinder. For further information about the characteristics of the configurations employed, the reader should refer to the original paper.

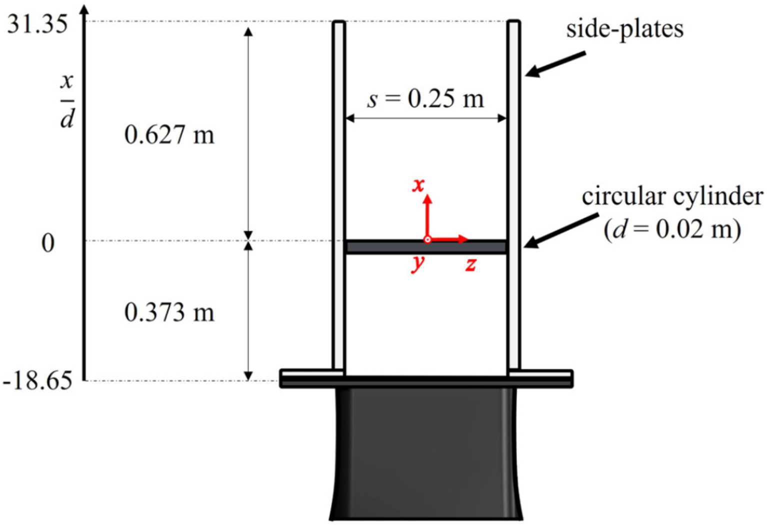

Figure 6.14: Test section showing the outlet nozzle, side plates, and cylinder specimen, including the reference system considered for presenting the results. Credits: *Zamponi et al.*

Regarding the acoustic measurements, they have been conducted using a microphone array of 64 G.R.A.S. 40 PH analog free-field microphones, each of them having a diameter of 0,007m and a lenght of 0,059m. The array (ref. fig. 6.15) is characterized by an aperture of around 2m and is arranged in a optimized multi-arm configuration that is oriented parallel to the $x-z$ plane, with the central microphone is located at $(x, y, z) = (5d,\ 59.25d,\ -0.25d)$. For each configuration, the data have been acquired at a sampling frequency of 102,4kHz for 20s. For the tests, five free-stream Reynolds numbers have been considered, namely, $\mathrm{Re}_d = 3.4\times10^4,\ 4.1\times10^4,\ 4.8\times10^4,\ 5.4\times10^4,\ 6.8\times10^4$, corresponding to free-stream flow

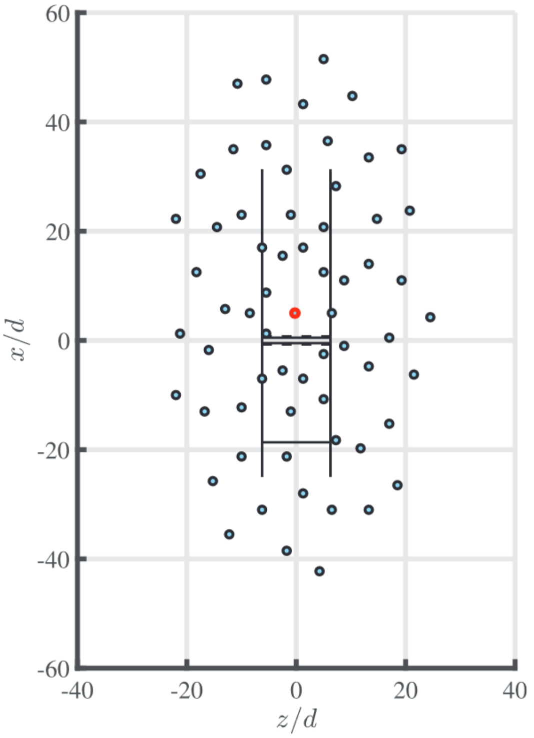

Figure 6.15: Relative position of the microphone array and the test section. The black lines indicate side plates, nozzle exit, and cylinder leading edge and trailing edge. The central microphone of the array is highlighted in red. Credits: *Zamponi et al.*

velocities u_0 ranging from $25\text{m}\,\text{s}^{-1}$ to $50\text{m}\,\text{s}^{-1}$.

6.3.2 Sound pressure levels (SPL) of the central microphone

The overall noise given by the presence of the cylinder can be associated with its effect on the array's central microphone, at a distance of 1m, that can be measured in terms of SPL using a $p_{\text{REF}} = 20\mu\text{Pa}$. In figure 6.16, the SPL trends over Strouhal number $\text{St} = \frac{fd}{u_0}$ for different configuration of the cylinder are reported, calculated for $\text{Re}_d = 4{,}1 \times 10^4$. It can be seen that all the configurations considered have a *lowering effect on the peak associated with the aeolian tone*. In addition, the *peak frequency is lowered*, and this appears to be due to the thickness that the coating introduces to the resulting configuration. The same conclusions are drawn for the other Reynolds numbers considered in the study.

6.3.3 GIBF settings

CSM matrix has been computed using the data collected at a free-stream velocity $u_0 = 50\text{m}\,\text{s}^{-1}$ (corresponding to $\text{Re}_d = 6.8 \times 10^4$) with Welch's method, with blocks of 2^{13} samples, corresponding to 0.16s, windowed through a Hanning weighting function that has 50% of data overlap, that results in a spectrum having a frequency resolution of 12.5Hz. The *convected monopole* reference solution (see sec. 4.5) is used due to the characteristics of the planar

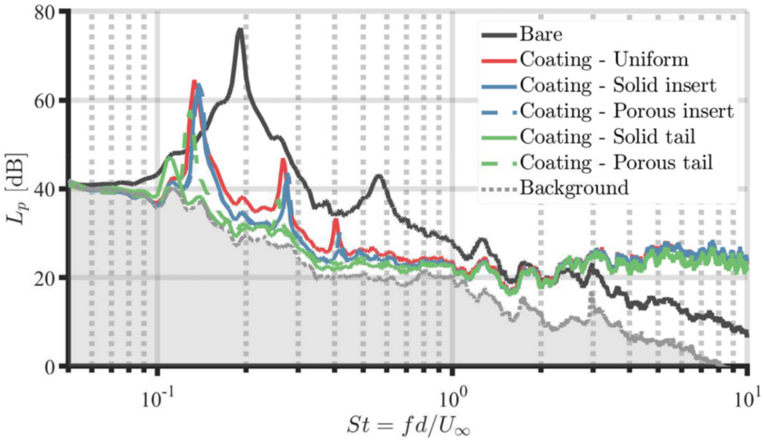

Figure 6.16: Absolute SPLs for the bare cylinder and the other cylinder configurations, relative to $\mathrm{Re}_d = 4{,}1 \times 10^4$, as measured by the array's central microphone, computed for $p_{\mathrm{REF}} = 20\mu\mathrm{Pa}$. Credits: *Zamponi et al.*

Grid description	
Dimensions	1m × 1m
Plane	$x - z$
Origin	$(0, 0, 0)$m
Resolution	30 sources/m
Number of sources	900

Table 6.5: Characteristics of the point grid adopted in GIBF *tool*.

array implemented, that would hardly discern a monopole from a y-dipole. The 1m × 1m grid employed (described in tab. 6.5 and shown in fig. 6.17) lies on the $x - z$ plane and features a resolution of 30sources/m, with a total number of 900 point sources. Regarding the parameters involved in the IRLS inversion algorithm, a $\mathcal{L}^1$ norm of the solution is minimized using a reduction factor of $1 - \beta = 5\%$ at every iteration until a minimum number of $N/2$ sources is reached. The value of ε is chosen to best match the resulting SPL of estimation with the central microphone's SPL trend. The sound maps in fig. 6.18 are generated for the bare and the coated cylinder case in the one-third frequency band of $f_{1/3} = 1.6$kHz to showcase the dominant source's shifting effect caused by the coating, a thing that explains the peak noise reduction for the coated cylinder observed in fig. 6.16.

6.3.4 Results

The GIBF *tool* proved to be essential in finding the position of the dominant sources, identifying an *actual shift of the sources downstream* in the case of the *coated cylinder*, which can explain the lowering of the perceived noise compared to the *bare* case. This can be seen well in the figure 6.18, where the dominant sources in the wake are observed on location $x/d = 2.5$ for the baseline cylinder (a) and on $x/d = 7.5$ for the coated one. These positions roughly correspond to the onset locations of the vortex shedding motion and thus represent

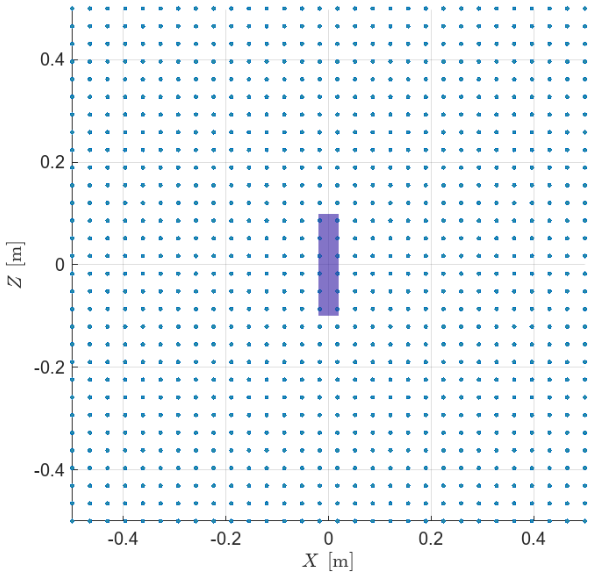

Figure 6.17: Visualization of the point grid employed for the beamforming analysis. Parameters are described in tab. 6.5.

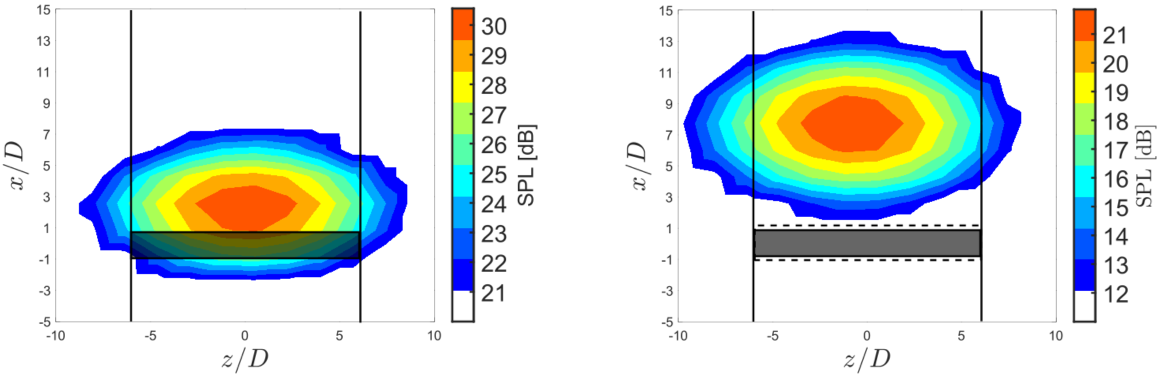

(a) Bare cylinder

(b) Coated cylinder (80PPI)

Figure 6.18: GIBF source reconstruction ($\varepsilon = 10\%$) using monopole formulation. Sound maps for (a) the baseline and (b) the cylinder uniformly coated with metal foam at $f_{1/3} = 1{,}6$kHz and $\mathrm{Re}_d = 6{,}8 \times 10^4$, $\mathrm{St} = 0{,}64$ computed with a reference pressure of 20µPa

high flow-mixing regions (due to shear layer instabilities), which explains the noise emission. The ability of porous coatings and other devices to delay the onset of these instabilities further downstream results in a *less intense scattering of acoustic waves on the cylinder*, which results in a *less efficient noise generation mechanism.*

Regarding the reconstruction of the source strength, it resulted to be unsatisfactory due to an *overestimation* of SPL values (ref. fig. 6.19), even when using the largest regularisation parameter $\varepsilon = 10\%$ in the range given by Suzuki. This emphasizes the necessity for a *more robust regularisation procedure* when using the GIBF *tool* to separate and quantify source contributions.

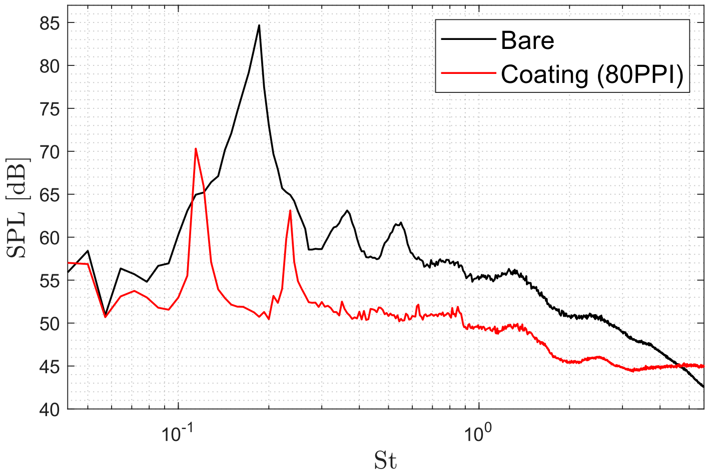

Figure 6.19: GIBF prediction of cylinder's emitted noise for the two configurations based on the propagation of map-integrated resolved sources, obtained for $\varepsilon = 10\%$. One can notice that GIBF predicted noise substantially follows the trends of the measured spectra reported in fig. 6.16, but definetely exceedes them in value, with a +5dB increase.

Chapter7

CONCLUDING REMARKS

A source imaging tool for Aeroacoustic applications, based on the Generalized Inverse Beamforming (GIBF) technique, has been successfully developed and implemented in a fully vectorized and parallelized MATLAB application equipped with a graphical interface. The tool has proven to effectively address the challenges associated with aeroacoustic measurements, both in wind tunnel environments and numerical simulations (CAA).

The adoption of GIBF has enabled overcoming the limitations of conventional beamforming, which relies on the assumption that the interrogation region solely contains sources within the domain—a hypothesis that becomes invalid when dealing with aeroacoustic problems. This was achieved by *simultaneously solving for all sources* in the acoustic field, inherently accounting for interference arising from the presence of *spatial distributions of coherent and incoherent sources.* Moreover, the ability to promote spatial sparsity in the solution through $\mathcal{L}^p$ norm minimization has facilitated the generation of *highly resolved and easily integrable acoustic maps.*

Regarding *wind tunnel measurements*, the propagation of acoustic sources has been formulated to consider the convection of sources due to the mean flow velocity and the presence of the shear layer in open-jet configurations. In addition to these benefits, concerning measurements based on CAA *simulations*, they have been maximized by implementing a formulation for the source-receiver propagation that is fully three-dimensional, thereby enabling 3D *beamforming in spatial domains* through multidimensional microphone arrays.

Furthermore, alongside *monopole beamforming*, *dipole-beamforming* has been introduced through a novel *multipole detection algorithm*, which, when applicable with the microphone array, has yielded excellent results in terms of localizing *freely oriented dipoles in space.*

In conclusion, GIBF *tool* definitely proved to be an important instrument for acoustic imaging purposes, *always delivering a fine reconstruction of the source distribution.* However, the regularization strategy adopted for the inverse problem, based on *heuristic selection of a regularization parameter*, has not yielded satisfactory results. It consistently overestimated (*monopole-beamforming*) or underestimated (*dipole-beamforming*) the peak SPL value predicted by GIBF in every benchmark, although accurately reproducing SPL spectra with varying frequencies.

A feasible approach for solving the issue could be represented by the *iterative Bayesian Focusing* (iBF) proposed by Antoni [31], that, based on statistical considerations, allows for informing the solver about regions where sources might be located. This strategy has proven capable of providing excellent results in terms of resolution and quantification, making it suitable for implementation as a *future development* of the GIBF *tool*.

BIBLIOGRAPHY

[1] T. Münzel et al. "Environmental Noise and the Cardiovascular System." In: *Journal of the American College of Cardiology* 71 6 (2018), pp. 688–697. DOI: `10.1016/j.jacc.2017.12.015`.

[2] European Environment Agency. *Environmental noise in Europe, 2020.* DOI: `10.2800/68624`. URL: `https://www.eea.europa.eu/`.

[3] S. Stansfeld et al. "Aircraft and road traffic noise and children's cognition and health: a cross-national study". In: *The Lancet* 365 (2005), pp. 1942–1949. DOI: `10.1016/S0140-6736(05)66660-3`.

[4] *On the establishment of rules and procedures with regard to the introduction of noise-related operating restrictions at Union airports within a Balanced Approach.* Regulation N°598/2014 of the European Parliament and of the Council. 2014.

[5] ICAO. *Convention on International Civil Aviation - Annex 16, 9th edition.* 2006. URL: `https://www.icao.int/`.

[6] *Fly the Green Deal, Europe's Vision for Sustainable Aviation, Report of the Advisory Council for Aviation Research and Innovation in Europe (ACARE).* URL: `https://www.acare4europe.org/`.

[7] T. Suzuki. "L1 generalized inverse beam-forming algorithm resolving coherent/incoherent, distributed and multipole sources". In: *Journal of Sound and Vibration* (2011). DOI: `10.1016/j.jsv.2011.05.021`.

[8] R. Zamponi, D. Ragni, S. van der Zwaag, and F. Avallone. "Innovative coatings for reducing flow-induced cylinder noise by altering the sound diffraction". In: *Physics of Fluids* (2023). DOI: `10.1063/5.0177263`.

[9] X. Gloerfelt, F. Pérot, C. Bailly, and D. Juvé. "Flow-induced cylinder noise formulated as a diffraction problem for low Mach numbers". In: *Journal of Sound and Vibration* (2005).

[10] R.K. Amiet. "Noise due to turbulent flow past a trailing edge". In: *Journal of Sound and Vibration* (1976), pp. 387–393. DOI: `10.1016/0022-460X(76)90948-2`.

[11] R.K. Amiet. “Acoustic radiation from an airfoil in a turbulent stream”. In: *Journal of Sound and Vibration* (1975). DOI: `10.1016/S0022-460X(75)80105-2`.

[12] M.J. Lighthill. “On sound generated aerodynamically I. General theory”. In: *Proceedings of the Royal Society of London. Series A. Mathematical and Physical Sciences* (1952).

[13] N. Curle. “The influence of solid boundaries upon aerodynamic sound”. In: *Proceedings of the Royal Society of London. Series A. Mathematical and Physical Sciences* (1955).

[14] J.E. Ffowcs Williams and D.L. Hawkings. “Sound generation by turbulence and surfaces in arbitrary motion”. In: *Philosophical Transactions of the Royal Society of London. Series A, Mathematical and Physical Sciences* (1969). DOI: `10.1098/rsta.1969.0031`.

[15] S. Glegg and W. Devenport. *Aeroacoustics of low mach number flows.* London: Elsevier Academic Press, 2017. ISBN: 9780128096512.

[16] T.J. Mueller. *Aeroacoustic measurements.* Springer Science & Business Media, 2002.

[17] S. Lee. “The use of equivalent source method in computational acoustics”. In: *Journal of Computational Acoustics* (2017). DOI: `10.1142/S0218396X16300012`.

[18] R. Zamponi, N. Van de Wyer, and C. Schram. “Benchmark assessment of an improved Regularization technique for generalized inverse beamforming”. In: *2018 AIAA/CEAS Aeroacoustics Conference.* 2018. DOI: `10.2514/6.2018-4106`.

[19] R. Zamponi. “Investigation of turbulence-surface interaction noise mechanisms and their reduction using porous materials”. PhD thesis. 2021.

[20] A. Dinsenmeyer, Antoni J, Q. Leclere, and A. Pereira. “On the denoising of cross-spectral matrices for (aero) acoustic applications”. In: *BeBec 7th Berlin Beamforming Conference.* 2018.

[21] Jørgen Hald. “Denoising of cross-spectral matrices using canonical coherence”. In: *The Journal of the Acoustical Society of America* (2019). DOI: `10.1121/1.5116010`.

[22] Y. Liu, A.R. Quayle, A.P. Dowling, and P. Sijtsma. “Beamforming correction for dipole measurement using two-dimensional microphone arrays”. In: *The Journal of the Acoustical Society of America* (2008). DOI: `10.1121/1.2931950`.

[23] P. Sijtsma. “Phased array beamforming applied to wind tunnel and fly-over tests”. In: *National Aerospace Laboratory NLR* (2010).

[24] R.K. Amiet. “Refraction of sound by a shear layer”. In: *Journal of Sound and Vibration* (1978). DOI: `10.1016/0022-460X(78)90353-X`.

[25] C. Colangeli, P. Chiariotti, and K. Janssens. “Uncorrelated noise sources separation using inverse beamforming”. In: *Experimental Techniques, Rotating Machinery, and Acoustics, Volume 8: Proceedings of the 33rd IMAC, A Conference and Exposition on Structural Dynamics.* Springer. 2015. DOI: `10.1007/978-3-319-15236-3_5`.

[26] P.C. Hansen. “Regularization tools: A Matlab package for analysis and solution of discrete ill-posed problems”. In: *Numerical algorithms* (1994). DOI: `10.1007/BF02149761`.

[27] A. Rieder. “On the regularization of nonlinear ill-posed problems via inexact Newton iterations”. In: *Inverse Problems* (1999). DOI: `0266-5611/15/1/028`.

[28] P.J. Huber. *Robust statistics.* John Wiley & Sons, 2004.

[29] T. Sueki, T. Takaishi, M. Ikeda, and N. Arai. “Application of porous material to reduce aerodynamic sound from bluff bodies”. In: *Fluid dynamics research* (2010). DOI: `10.1088/0169-5983/42/1/015004`.

[30] H. Naito and K. Fukagata. “Numerical simulation of flow around a circular cylinder having porous surface”. In: *Physics of Fluids* (2012). DOI: `10.1063/1.4767534`.

[31] Jérôme Antoni, Thibaut Le Magueresse, Quentin Leclere, and Patrice Simard. “Sparse acoustical holography from iterated Bayesian focusing”. In: *Journal of Sound and Vibration* (2019). DOI: `10.1016/j.jsv.2019.01.001`.